



Amplified bottom water acidification rates on the Bering Sea shelf from 1970-2022

Darren J. Pilcher^{1,2}, Jessica N. Cross^{2,3}, Natalie Monacci⁴, Linqun Mu¹, Kelly A. Kearney^{1,5}, Albert J. Hermann^{1,2}, Wei Cheng^{1,2}

5 ¹ Cooperative Institute for Climate, Ocean, and Ecosystem Studies, University of Washington, Seattle, WA, USA

² NOAA Pacific Marine Environmental Laboratory, Seattle, WA, USA

³ Pacific Northwest National Laboratory, Sequim, WA, USA

⁴ University of Alaska Fairbanks, Fairbanks, AK, USA

⁵ NOAA Alaska Fisheries Science Center, Seattle, WA, USA

10

Correspondence to: Darren J. Pilcher (darren.pilcher@noaa.gov)

Abstract. The Bering Sea shelf supports a highly productive marine ecosystem that is vulnerable to ocean acidification (OA) due to the cold, carbon rich waters. Previous observational evidence suggests that bottom waters on the shelf are already seasonally undersaturated with respect to aragonite (i.e. $\Omega_{\text{arag}} < 1$), and that OA will continue to increase the spatial extent, duration, and intensity of these conditions. Here, we use a regional ocean biogeochemical model to simulate changes in ocean carbon chemistry for the Bering Sea shelf from 1970-2022. Over this timeframe, surface Ω_{arag} decreases by $-0.043 \text{ decade}^{-1}$ and surface pH by $-0.014 \text{ decade}^{-1}$, comparable to observed global rates of OA. However, bottom water pH decreases at twice the rate of surface pH, while bottom $[\text{H}^+]$ decreases at nearly three times the rate of surface $[\text{H}^+]$. This amplified bottom water acidification emerges over the past 25 years and is likely driven by a combination of anthropogenic carbon accumulation and a trend of increasing primary productivity and increasing subsurface respiration and remineralization. Due to this enhanced bottom water acidification, the spatial extent of bottom waters with $\Omega_{\text{arag}} < 1$ has greatly expanded over the past two decades, along with pH conditions harmful to red king crab. Interannual variability in surface and bottom Ω_{arag} , pH, and $[\text{H}^+]$ has also increased over the past two decades, resulting in part from the increased physical climate variability. We also find that the Bering Sea shelf is a net annual carbon sink of 1.1-7.9 TgC/year, with the range resulting from the difference in the two different atmospheric forcing reanalysis products used. Seasonally, the shelf is a significant carbon sink from April-October but a somewhat weaker carbon source from November-March.

15
20
25
30



1 Introduction

The global ocean presently absorbs 25-31% of annual CO₂ emissions, making it a critical
35 carbon sink that mitigates anthropogenic warming (Gruber et al., 2019; Friedlingstein et al.,
2020; McKinley et al., 2020). The uptake of this anthropogenic carbon has driven a shift in the
marine carbonate system towards a state of lower pH and carbonate saturation, a process referred
to as Ocean Acidification (OA; Feely et al., 2004). High latitude regions are particularly
vulnerable to OA due to the poorly buffered, cold temperature waters generating naturally low
40 carbonate saturation states (Fabry et al., 2009). Experimental studies have determined a number
of negative effects to marine organisms due to OA (Doney et al., 2020), particularly for
organisms that form calcium carbonate shells as these shells become harder to build and maintain
as carbonate saturation states (Ω) approach and drop below 1. Pteropod shell dissolution has
already been observed in several high-latitude environments (Bednarsek et al., 2012; Niemi et
45 al., 2021), and OA is expected to shift these conditions equatorward over time.

Although OA is driven by the increase in atmospheric CO₂ and subsequent increase in
ocean carbon uptake, there are a number of physical and biogeochemical processes that can
modify the rate of OA expected from the increase in atmospheric CO₂ (Hauri et al., 2021). For
example, the accumulation of respired carbon at depth reduces the buffer capacity of subsurface
50 water, leading to amplified subsurface acidification rates compared to surface waters throughout
large regions of the global oceans (Fassbender et al., 2023). Coastal shelf systems can
experience local rates of acidification much faster than the global oceans due to upwelling (Feely
et al., 2008), biological respiration (Feely et al., 2010), eutrophication (Laurent et al., 2017), and
changes in circulation (Siedlecki et al., 2021). In the Arctic, changes in sea ice formation (Zhang
55 et al., 2020) and biological productivity and remineralization (Qi et al., 2022) can generate
acidification rates 2-3 times greater than the rate for the open oceans.

The Bering Sea is composed of a relatively large (> 500km wide and > 100km long),
shallow eastern coastal shelf along with, a narrow western shelf, and a deep interior basin. The
shelf itself is composed of three distinct biophysical domains (inner, middle, and outer) often
60 delineated by the 50m, 100m, and 200m isobaths. General circulation on the shelf tends to follow
these isobaths in a north-northwest direction, eventually feeding into the western intensified
Anadyr Current, which then flows through Bering Strait, thereby providing a key conduit
between the Bering Sea and Arctic (Kinder et al., 1986; Stabeno et al., 2016). The Bering Sea



shelf ecosystem is strongly tied to the atmospheric and oceanic physical forcing, with the
65 seasonal formation and retreat of sea ice playing a fundamental role through the development of
the bottom water cold pool and by setting the timing and magnitude of the spring phytoplankton
bloom (Brown and Arrigo 2013; Sigler et al., 2014). While the formation of sea ice occurs
annually, the areal extent and timing of ice formation and retreat can vary substantially. This
variability during the past 10-20 years has consisted of multi-year periods of persistent warm,
70 low sea ice extent (e.g. 2001-2005 and 2014-2018) or cold, high sea ice extent conditions (e.g.
2007-2013; Stabeno et al., 2012). The recent warm years have generated record breaking low
sea ice extent and high temperatures in the northern Bering Sea, with substantial negative
impacts to the marine ecosystem (Stabeno and Bell, 2019; Siddon et al., 2020).

On annual timescales, the Bering Sea shelf is generally considered a net carbon sink,
75 driven by substantial spring-summer primary productivity generating low surface ocean $p\text{CO}_2$
values and a net influx of carbon from the atmosphere (Bates et al., 2011; Cross et al., 2014;
Pilcher et al., 2019). A portion of the carbon fixed by this mixed layer productivity sinks to
bottom waters where it is respired into inorganic carbon and can be re-emitted back to the
atmosphere in fall-winter due to strong atmospheric wind speeds and vertical mixing (Cross et
80 al., 2014; Pilcher et al., 2019). Sea ice further impacts the seasonal carbon cycle by acting as a
physical barrier inhibiting air-sea gas exchange. Furthermore, sea ice formation can pump DIC
and total alkalinity to the bottom along with salinity via brine rejection, while sea ice melt dilutes
both variables in surface waters (Mortenson et al., 2020).

Previous observational and modeling studies have found that seasonal periods of
85 undersaturation of aragonite ($\Omega_{\text{arag}} < 1$) are already occurring within subsurface waters and near
regions of significant riverine freshwater runoff (Mathis et al., 2011; Cross et al., 2013; Pilcher et
al., 2019). Subsurface $\Omega_{\text{arag}} < 1$ waters occur in summer and early fall, driven by bacterial
respiration associated with remineralization of sinking organic matter, particularly in regions of
high primary productivity in the middle and outer shelf domains (Mathis et al., 2011). Surface
90 waters generally maintain much higher values of Ω_{arag} and pH due to this significant primary
productivity, except near freshwater runoff, particularly the mouths of the Yukon and
Kuskokwim rivers, where $\Omega_{\text{arag}} < 1$ and relatively low pH values are driven by relatively high
DIC:TA ratios due to terrestrial carbon exports (Mathis et al., 2011; Pilcher et al., 2019).
Furthermore, model simulations suggest that winter surface Ω_{arag} values are relatively low and



95 close to 1, particularly in ice covered regions where entrained subsurface carbon cannot re-
equilibrate with the atmosphere (Pilcher et al., 2019). Winter observational data is extremely
sparse due to challenging weather and sea ice conditions; however, limited late-fall data suggest
supersaturated $p\text{CO}_2$ conditions (Cross et al., 2014; Cross et al., 2016). Model simulations
project that seasonal periods of surface Ω_{arag} undersaturation may grow to encompass up to 5
100 months of the year following the RCP 8.5 emissions scenario and 2-3 months following the RCP
4.5 scenario (Pilcher et al., 2022).

The Bering Sea sustains a substantial U.S. fishery, representing 40% of U.S. total fish
catch by weight and \$3 billion in annual value (Wiese et al., 2012). These fisheries also provide
commercial, subsistence, and cultural benefits to many Alaskan communities, putting them at
105 risk from ocean acidification (Mathis et al., 2015). In the Bering Sea, red and tanner crab have
emerged as species particularly vulnerable to the direct effects of OA. The growth rates and
survival of larval and juvenile crab for both species are decreased at lower pH values (Long et
al., 2013a,b; Long et al., 2016). Incorporating these results into bioeconomic models suggests
that the red king crab fishery could substantially decline if OA is not accounted for in the
110 fisheries management process (Seung et al., 2015; Punt et al., 2016). Recent closures of the
snow crab fishery and the Bristol Bay red king crab fishery have had devastating impacts to the
Bering Sea commercial fishing community and has led to some discussion concerning the
potential role of OA. However, recent laboratory studies have found that snow crab appear
resilient to OA (Algayer et al., 2023), and that the snow crab fishery collapse may be due to a
115 mass mortality event resulting from the 2018-2019 heatwave (Szuwalski et al., 2023). In
comparison to the collapse in snow crab populations, the Bristol Bay red king crab fishery has
been in a steady decline since 2014 (Fedewa et al., 2020). Although model results suggest that
bottom waters in parts of Bristol Bay have pH values harmful to larval and juvenile red king
crab, these crab populations tend to inhabit nearshore regions that are relatively well buffered
120 with much higher pH values (Pilcher et al., 2022). Thus, the potential role of OA in impacting
Bristol Bay red king crab populations is currently unclear.

Recent work utilized a regional ocean biogeochemical model and a dynamical
downscaling technique to generate long-term projections of OA for the Bering Sea shelf using
multiple Earth System Models (ESMs) and emissions scenarios (Pilcher et al., 2022). Here, we
125 greatly expand the temporal coverage of our previous model hindcast (e.g. Pilcher et al., 2019) to



simulate 53 years (1970-2022) of the Bering Sea marine carbon cycle. We use this model output to quantify spatial-temporal trends in Bering Sea shelf marine carbonate variables over the entire hindcast and the underlying mechanisms generating heterogeneity in these trends. We conclude by illustrating how this model output is being incorporated into the fisheries management process and the next steps to continue refining these model-based OA products.

2 Methods

2.1 Base model description

The regional Bering10K model is an implementation of the Regional Ocean Modeling System (ROMS; Shchepetkin and McWilliams, 2005; Haidvogel et al., 2008), with 10 km horizontal resolution and 30 vertical layers. The Bering10K model simulates sea ice formation and melt, along with tidal mixing. A thorough description of the physical model can be found in Hermann et al., (2016) and Kearney et al., (2020). This physical model is coupled to a lower trophic NPZD model, originally developed as part of the Bering Sea Ecosystem Study (BESTNPZ; Gibson and Spitz 2011), and recently updated by Kearney et al., (2020). Briefly, the BESTNPZ model simulates two phytoplankton groups (small and large), five zooplankton groups (microzooplankton, small copepods, large copepods, euphausiids, and jellyfish), three nutrient groups (nitrate, ammonium, iron), and two detrital groups (slow and fast sinking). BESTNPZ also contains an ice biology sub-model which simulates ice algae, nitrate, and ammonium, along with a benthic sub-model which simulates a benthic infauna group and a detrital group. A thorough description of the BESTNPZ model can be found in Kearney et al., 2020.

Carbonate chemistry is incorporated into the Bering10K BESTNPZ model by simulating dissolved inorganic carbon (DIC) and total alkalinity (TA), which are used to calculate the remainder of the carbonate system following the OCMIP-2 protocols (Orr et al., 1999) and CO2SYS (Lewis and Wallace, 1998). Here we report pH and $[H^+]$ values on the total scale. DIC is generated from planktonic respiration and detrital remineralization, and consumed via planktonic photosynthesis. Additionally, DIC is exchanged with the atmosphere depending on the gradient in the partial pressure of CO_2 between the surface ocean and the atmosphere ($DpCO_2$) and the wind speed following Wanninkhof et al., (2014). The atmospheric CO_2 concentration is set to the monthly in-situ concentration from Barrow, Alaska (Thoning et al.,



2022). This timeseries started in 1973; for 1970-1972, we take the 1973 Barrow monthly
timeseries and subtract the respective annual growth rate from the Mauna Loa timeseries
(<https://gml.noaa.gov/ccgg/trends/>). Riverine freshwater runoff flux is prescribed following
160 freshwater discharge data from Alaska and Russia (Kearney, 2019). This river runoff contains
seasonally varying concentrations of DIC and TA following data collected at Pilot Station at the
mouth of the Yukon River (Striegl et al., 2007; PARTNERS, 2010, Pilcher et al., 2019).

The atmospheric forcing for air temperature, sea level pressure, longwave and shortwave
radiation, u and v winds, specific humidity, and rainfall are provided by a combination of
165 reanalysis products. For 1970-1994 we use the Common Ocean Reference Experiment (CORE;
Large and Yeager, 2009) forcing, for 1995-2011 the Climate Forecast System Reanalysis (CFSR;
Saha et al., 2010), and for 2011-2021 the Climate Forecast System Operational Analysis
(CFSv2-OA; Saha et al., 2014). Lateral open boundary conditions at weekly resolution for
temperature, salinity, and oceanic velocities (u and v) are derived from the larger scale Northeast
170 Pacific model (Danielson et al., 2011) for the CORE forcing timeframe, and the CFSR/CFSv2-
OA for CFSR forcing timeframe. Nitrate boundary conditions are monthly climatologies from a
long-term run of the larger Northeast Pacific (NEP-5) ROMS domain (Danielson et al., 2011).
Oxygen initial conditions and monthly boundary conditions are climatologic means from the
World Ocean Atlas 2018 product (Garcia et al., 2018). Water column iron concentrations are
175 nudged towards empirical climatological profiles.

The lateral boundary conditions for DIC and TA are calculated via linear regressions with
salinity, derived from observational data collected primarily from 2008-2010 (Pilcher et al.,
2019). The salinity-DIC regression has changed over time as the oceanic uptake of CO₂ has
increased the DIC concentration of waters, with no effect on salinity. Thus, using this same
180 relationship for the boundary conditions at the start of the hindcast in 1970 would introduce a
high DIC bias. To account for changes in DIC over time, we center the DIC-salinity relationship
on the year 2009 (i.e. midpoint of 2008-2010 sampling timeframe) and subtract (add) DIC for
years before (after) 2009. The DIC value added or subtracted is calculated from the linear trend
in DIC calculated from the historical runs of the Coupled Model Intercomparison Phase 6
185 (CMIP6) over the 1970-2009 timeframe from the mean of three different Earth System Models.
These three ESMs were selected as they have been coupled previously with the Bering10K



regional model (Cheng et al., 2021; Pilcher et al., 2022). We chose to use this method to gain the higher spatial resolution, particularly in the vertical, provided by the ESM output.

Initial conditions for the start of the hindcast in 1970 for non-carbonate chemistry
190 variables are taken from a 30-year model spin-up using repeating 2001 forcing (Kearney et al., 2020). Initial conditions for TA are calculated using the same salinity regression used for the boundary conditions. Similarly, the DIC initial conditions use the salinity regression, along with subtracting the same long-term trend used for the boundary conditions. The model is then spun-up for an additional three years using repeating 1970 forcing, at which point the model seasonal
195 CO₂ cycle was approximately in balance with minimal year-to-year on-shelf variations. The model hindcast is then started and run continuously for 1970-2022.

2.2 Model updates

A new addition to the BESTNPZ model presented in previous work is the inclusion of
200 oxygen cycling following Siedlecki et al., (2015) and Bianucci et al., (2011). Oxygen cycling contains phytoplankton growth as a source, and respiration, remineralization, and nitrification as sinks. Oxygen cycling throughout the water column is governed by the following equation:

$$\frac{\partial O_2}{\partial t} = \text{Phy}_i * u_i(\text{Light}, N) - \text{resp}(\text{Phy}_i) - \text{resp}(Z_i) - \text{remin}(D_i) - \text{Nitrification} \\ + \text{advection} + \text{diffusion}$$

205 (1)

Surface and bottom oxygen concentrations are further modified through the following equations, respectively:

$$\left. \frac{\partial O_2}{\partial t} \right|_{\text{surface}} = \frac{V_{O_2}}{\Delta Z} * ([O_2]_{\text{sat}} - [O_2]_{z=\text{surface}})$$

210 (2)

$$V_{O_2} = 0.251u^2 \left(\frac{S_c}{660} \right)^{-0.5}$$

(3)



$$\left. \frac{\partial O_2}{\partial t} \right|_{Bottom} = \frac{1}{\Delta z} \left(W_D \left. \frac{dD}{dz} \right|_{z=Bottom} \right) - resp(Ben) - excretion(Ben) - remin(DetBen) \quad (4)$$

215 where Phy_i is the phytoplankton group, u_i is the growth rate, $Light$ and N and the light and nutrient limitations respectively, $resp$ is respiration, Zi is the zooplankton group, $remin$ is bacterial remineralization, and D_i is the detrital group. For the surface equation (2), Δz is the vertical thickness of the grid cell, $[O_2]_{sat}$ is calculated following the equation from Garcia and Gordon (1992), S_c is the Schmidt number, and V_{O_2} is the gas transfer velocity following
220 Wanninkhof (2014). For the bottom equation (4), W_D is the detrital sinking rate, Ben is the benthic infauna group, and $DetBen$ is benthic detritus. The above model equations (1-4) utilize constant stoichiometric molar ratios consisting of C:N = 106:16, O_2 :N = 138:16 for nitrate fluxes, and O_2 :N = 106:16 for ammonium fluxes. The complete BESTNPZ model equations are found in Kearney et al., (2020).

225

2.3 Observational data for model validation

To assess overall model skill, we compare model hindcast output to several observational datasets. One of the largest available datasets for carbonate chemistry in the Bering Sea was collected and compiled during the 2008-2010 Bering Sea Ecosystem Study (BEST) and Bering
230 Sea Integrated Research Program (BSIERP). This dataset is particularly valuable due to the large number of discrete DIC and TA samples; these are the prognostic model variables used within the model and therefore provide a direct model-data comparison. These data were typically collected in the spring (April/May) and summer (June/July) seasons, along with a fall (September/October) sample period in 2009. The sampling regime covered a large portion of the
235 U.S. southeastern Bering Sea shelf, including three cross-shelf transects (Fig. 1). pCO_2 , pH, and Ω_{arag} values were calculated from DIC, TA, salinity, and temperature measurements using CO2SYS (Cross et al., 2012; Cross et al., 2013).

The M2 mooring is the longest dataset for surface ocean pCO_2 in the Bering Sea. While the M2 mooring itself provides a multi-decadal long timeseries of standard oceanographic
240 properties, the moored autonomous surface vehicle (MAPCO2; Sutton et al., 2019) system used to measure pCO_2 was first deployed in 2013 and has since been re-deployed with the M2 mooring during the ice-free season for every year except 2020. Generally, this timeseries covers



the months of May-September, however in 2021 it was left out much later than usual, providing the first glimpse of late fall and early winter $p\text{CO}_2$. For further model validation of $p\text{CO}_2$, we also utilize $p\text{CO}_2$ measurements from an Autonomous Surface Vehicle CO_2 System (ASVCO2)

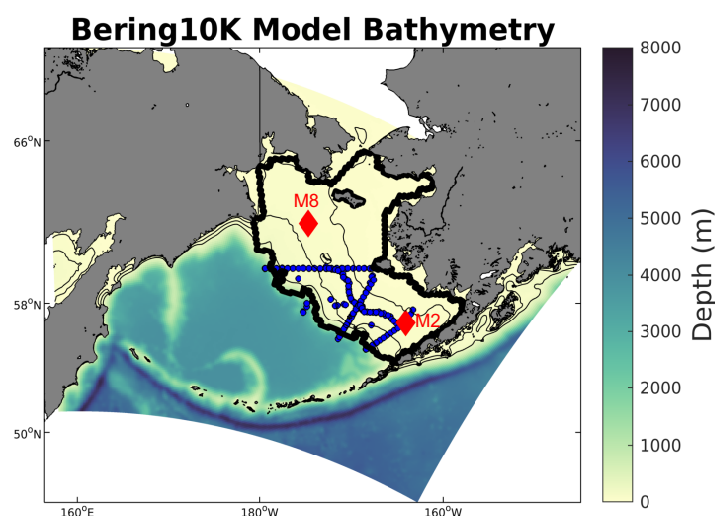


Figure 1: Spatial map of the model domain along with the model bathymetry. Also shown are the discrete ship-based sample locations (blue dots) and the two moorings (red diamonds) used for model validation. The black line denotes the spatial region used to encompass the Bering Sea shelf.

onboard the Saildrone uncrewed surface vehicle (USV) (Wang et al., 2022). This dataset provides a transect of surface ocean $p\text{CO}_2$, generally running from the Aleutian Islands to the Bering Strait during missions to the Chukchi Sea from 2017-2019. Therefore, each year contains a northward transect in late spring/early summer, along with a southward transect in late summer.

255

3 Results

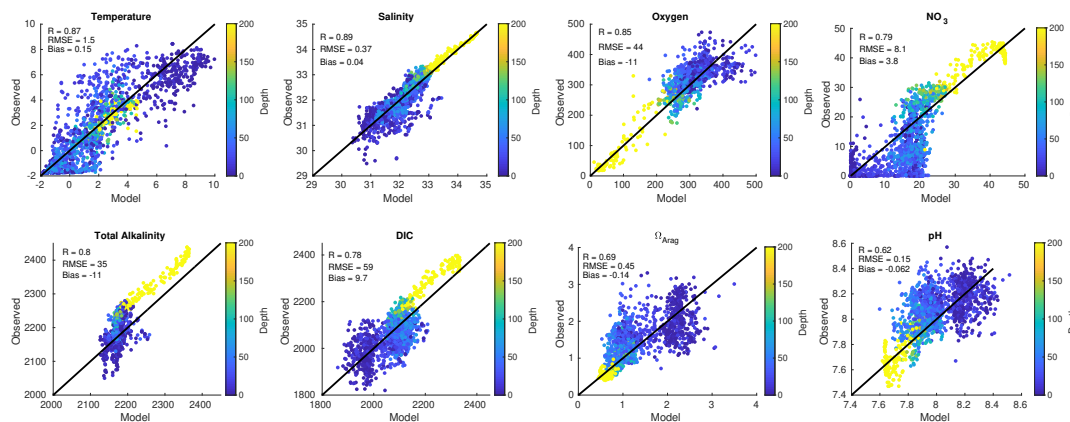
3.1 Model Skill Assessment

Model property-property comparisons and associated skill statistics between discrete samples collected during 2008-2010 and the model hindcast illustrate relatively high correlation coefficients across the water column for most model prognostic variables (Fig. 2). However, a slight negative TA bias combined with a slight positive DIC bias work synergistically to generate a relatively larger negative bias in Ω_{arag} and pH. Another notable model-data mismatch is that subsurface points (depth > 200m) for salinity, NO_3 , TA, and DIC are all relatively lower in the model compared to the observations. These points are all outside of our definition of the Bering

260



265 Sea shelf (encompassing depth 0-200m; Fig. 1) and are located on the shelf break, which is smoothed in the model bathymetry to ensure numerical stability (Kearney et al., 2020).



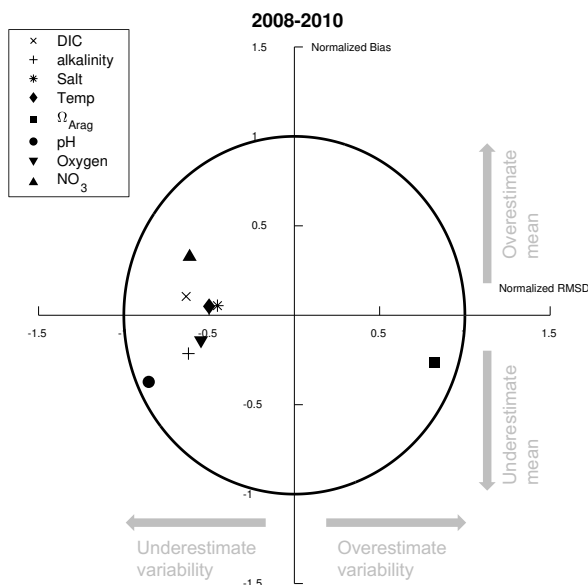
270 **Figure 2:** Plots of model (x-axis) and observed (y-axis) co-located points for different model variables. Also shown in each plot are the R, RMSE, and bias skill statistics. Observed data are from the 2008-2010 BEST-BSIERP project, shown as blue dots in Fig. 1. Note that here the colorbar is constrained to depths between 0-200m because our focus is on the shelf, though deeper, off-shelf points (denoted by bright yellow dots) are still included.

The model-data comparison illustrated in Fig. 2 is further summarized via a Target Diagram (Jolliff et al., 2009) in Fig. 3. In a Target diagram, the position in the y-axis denotes either a positive ($Y > 0$) or negative ($Y < 0$) normalized model bias, while the position in the x-axis signifies whether the model has a larger ($X > 0$) or smaller ($X < 0$) root-mean-square-deviation (RMSD) compared to the observed data. The radial distance from the origin (normalized RMSD) is then related to the modeling efficiency metric (MEF; Stow et al., 2009), where model variables that lie within the RMSD < 1 circle have a MEF > 0, signifying that the model outperforms an estimate based solely on the mean of the observations. Figure 3 illustrates that all highlighted model variables fall within the RMSD value of 1, with relatively low overall biases. Most model variables display less variability compared to the observations, except for Ω_{arag} which displays more variability.

In addition to the ship-based observational comparison, model output of surface ocean $p\text{CO}_2$ is also compared to the M2 mooring timeseries (Fig. 4). The model accurately captures the timing of the late spring $p\text{CO}_2$ drawdown along with the subsequent increase in $p\text{CO}_2$ leading into summer. Furthermore, the modeled late fall and early winter increase in $p\text{CO}_2$ is also apparent in the mooring for the single year that the mooring was left out late into the season. However, the model generally tends to underestimate the magnitude of the late spring $p\text{CO}_2$ drawdown, which then subsequently leads to model overestimations of summer $p\text{CO}_2$. Notable



290 exceptions are apparent in 2013, 2018, and 2022 when the observed late spring $p\text{CO}_2$ drawdown was relatively weaker, and the modeled drawdown is more comparable with observations.



295 **Figure 3:** Target diagram summarizing the data comparison from Fig. 2. Here, the X-axis is the normalized unbiased RMSD between the model and data, multiplied by the sign of the difference between model and observed standard deviation. The Y-axis is the normalized mean bias.

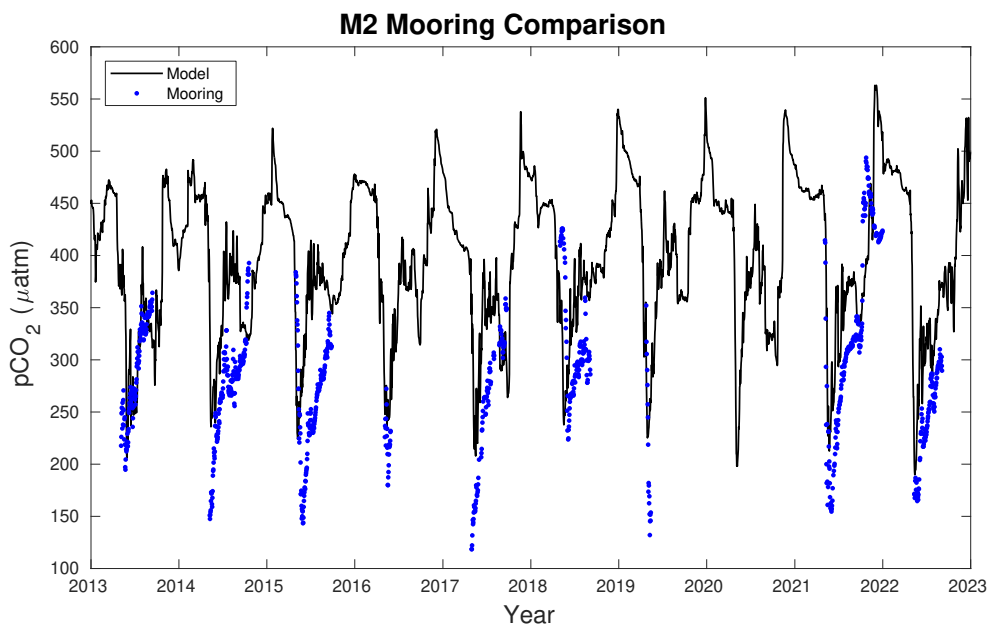


Figure 4: M2 mooring $p\text{CO}_2$ data (blue dots) compared to model daily $p\text{CO}_2$ values (black line) at the equivalent model grid cell location. The mooring is generally deployed in spring and retrieved in fall, though was out much later in 2021.



Further surface $p\text{CO}_2$ comparisons between the model output and in-situ $p\text{CO}_2$ from the
 300 autonomous Saildrone platform are shown in Fig. 5. Overall, the model does a reasonably

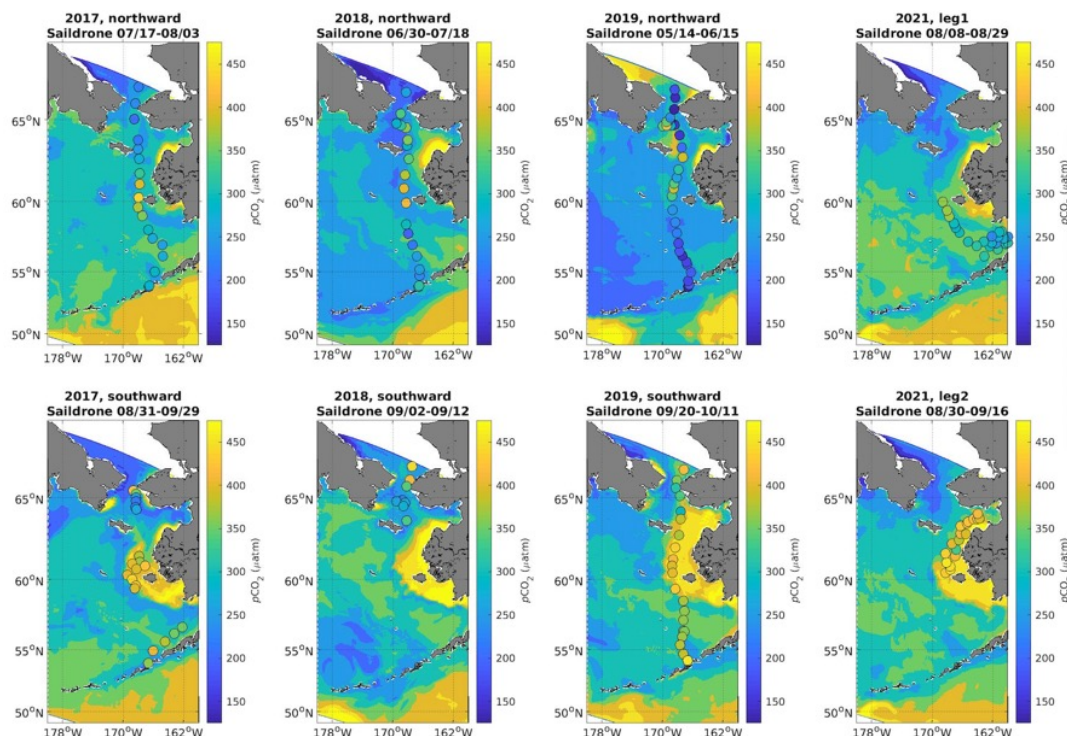


Figure 5: Surface $p\text{CO}_2$ values from Saildrone transects (dots) with model surface $p\text{CO}_2$ values averaged over the equivalent timeframe as the background shading.

sufficient job of capturing the dominant spatial pattern in $p\text{CO}_2$ illustrated by the Saildrone data,
 305 namely the relatively lower $p\text{CO}_2$ values in the southeastern and northern Bering Sea with higher
 values in the central inner shelf domain near Nunivak Island. The seasonality between the two
 transects also aligns, with relatively lower values during the northward transect and higher values
 during the southward transect. However, the model appears to consistently underestimate the
 $p\text{CO}_2$ drawdown (i.e. model $p\text{CO}_2$ biased high compared to Saildrone data) in the southeastern
 310 Bering Sea during the northward transect, similar to the underestimated spring $p\text{CO}_2$ drawdown
 from the M2 mooring comparison (Fig. 4). However, the southward transects suggest that this
 bias is reversed later in the year, where the model is now biased low compared to the Saildrone
 data, which is also the opposite bias of what we see during the late summer and early fall in the
 M2 mooring comparison. Additionally, the model tends to underestimate $p\text{CO}_2$ in the central
 315 inner shelf domain just to the west of Nunivak Island. It appears that the Saildrone data is



consistently capturing a relatively high plume of $p\text{CO}_2$ in this region. The model also generally simulates these relatively high $p\text{CO}_2$ waters in that region of the inner shelf domain, but there is a lot of interannual variability and seasonality in this feature.

This analysis suggests that the model is simulating the Bering Sea carbon cycle reasonably well, though there are some noted differences. Namely, the model appears to underestimate variability overall (Fig. 3) and underestimate the magnitude of the seasonal $p\text{CO}_2$ drawdown according to both the M2 mooring and Saildrone data. This could be due to a somewhat smaller magnitude spring bloom, which is consistent with slight positive model biases in DIC and NO_3 from the ship-based observation comparison (Fig. 2). This bias could translate to model pH and Ω_{arag} values that are biased low in surface waters but biased high in bottom waters, due to less respiration of sinking organic carbon from a smaller spring bloom. However, we caution that bottom measurements are very limited overall, and were all collected during the anomalously cold-water conditions during 2008-2010. Furthermore, $p\text{CO}_2$ is a relatively difficult variable for the model to capture because it is a nonlinear, diagnostic variable that is dependent on temperature, salinity, DIC, and TA. This nonlinearity and the potential for synergistic biases (e.g. positive DIC bias but negative TA bias) can generate very large magnitude deviations. Thus, additional bottom water data, particularly for DIC and TA, would be extremely useful in further validating the bottom water carbonate chemistry beyond the 2008-2010 analysis here.

335

3.2 Impact of forcing on linear trends

The Bering10K BESTNPZ model has historically been utilized for a variety of fisheries management applications (Gibson and Spitz, 2011; Kearney et al., 2020). For these applications, the model hindcast timeframe needed to run through the present and extend back in time to cover major transitions in the Bering Sea during the 1970s and 1980s. No individual forcing product provided this full timeframe, therefore, it was necessary to combine the CORE and CFSR forcing. Furthermore, the transition between products in 1995 was selected as the 1990s experienced relatively more stable climate variability for the Bering Sea, as this was after the shifts in the 1970s and 1980s, but prior to the temperature stanzas of the early 2000s (Stabeno et al., 2012). However, any significant differences in either the atmospheric forcing or the oceanic boundary conditions between the datasets could generate a significant deviation in model results,

340
345



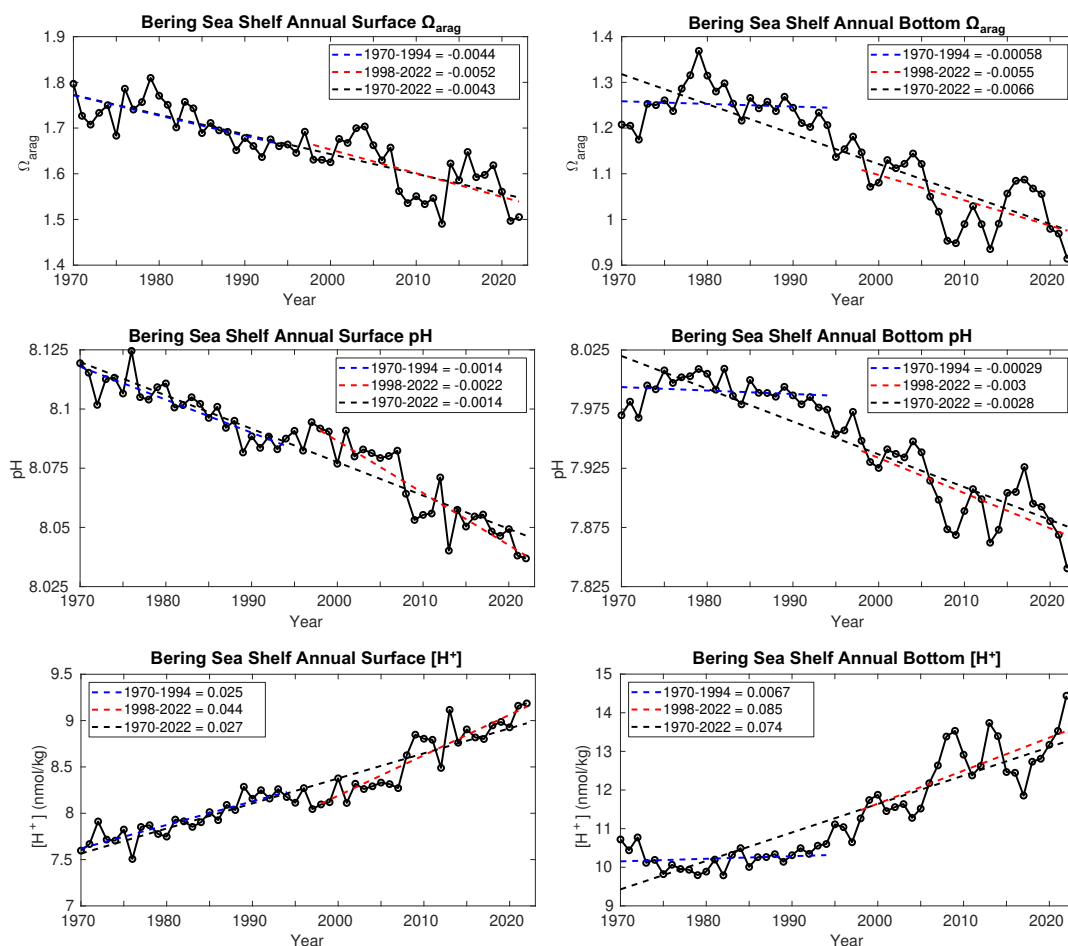
particularly immediately following the transition in 1995. Furthermore, this transition (i.e. essentially a spin-up to the new model forcing) could generate erroneous linear trends when calculated over the entire timeframe, that would represent a shift in the variable over a discrete
350 period, rather than a multi-decadal trend. To help clarify this potential influence, we ran a separate simulation which branched off from the primary hindcast simulation in 1995 by continuing the CORE forcing until 2003. We then compared these results to the primary hindcast simulation (e.g. simulation that switches to CFSR in 1995) to assess the effect of this transition in forcing.

355 Surface and bottom salinity for the Bering Sea shelf provides an example of how the shift in forcing can generate an erroneous long-term trend. A noticeable decrease in salinity of ~ 0.5 psu immediately follows the switch to CFSR forcing and oceanic boundary conditions, which does not occur when the CORE forcing and northeast Pacific model derived oceanic boundary conditions are extended to 2003 (Fig. S1). This decrease generates a negative trend in surface
360 salinity when calculated over the entire timeframe, however, trends over the individual forcing timeframes are extremely weak and of the opposite sign for the CORE timeframe.

To account for the potential influence of this transition in forcing, we report all timeseries linear trends over three timeframes: 1.) the complete 1970-2022 CORE-CFS timeframe, 2.) the 1970-1994 CORE timeframe, and 3.) the 1998-2022 CFSR timeframe. We start the CFSR trends
365 in 1998 rather than 1995 to account for several years for the transition in forcing, based in part on the re-equilibration to the new forcing by 1998 demonstrated in salinity (Fig. S1). Furthermore, dividing the hindcast into the two timeframes of 1970-1994 and 1998-2022 produces two, equivalent 25-year time slices and will help elucidate any acceleration in trends. Lastly, we show the results of the CORE simulation extended to 2003 for trend estimates in the
370 supplementary information, noting which variables exhibit consistent trends throughout both forcing datasets, and which variables' long-term trends (estimated over 1970-2022) are impacted by the forcing switch in 1995.

3.3 Bering Sea Shelf Acidification

375 Over the 1970-2022 model hindcast, annual surface and bottom Ω_{arag} and pH decrease, while $[\text{H}^+]$ increases for the Bering Sea shelf, with linear trends greater at the bottom compared



380 **Figure 6:** Timeseries plots of model annual average surface (left) and bottom (right) Ω_{arag} (top), pH (middle), and $[H^+]$ bottom averaged over the Bering Sea shelf region. Also shown are the linear trend values over three different timeframes.

to the surface (Fig. 6). We show $[H^+]$ in addition to pH because pH changes reflect relative $[H^+]$ changes and are, therefore, not ideal for comparisons between waters with different initial chemistry conditions, such as between surface and bottom waters (Fassbender et al., 2017; Fassbender et al., 2021). Surface Ω_{arag} ranges from 1.7-1.8 at the start of the simulation and
 385 decreases to 1.5-1.6 by the end, surface pH ranges 8.1-8.125 and decreases to 8.025-8.05, and surface $[H^+]$ ranges from 7.5-7.75 nmol/kg at the start and increases to 9.25 nmol/kg by 2022. Furthermore, the bottom pH trend from 1970-2022 is twice as great as the surface trend, while the bottom $[H^+]$ trend over the same timeframe is nearly three times as great as the surface $[H^+]$ trend. In fact, bottom acidity, as denoted by $[H^+]$, increases by approximately 40% from 1970-
 390 2022. These amplified bottom water carbonate trends are driven by the more recent timeframe,



as trends over the CORE-forced 1970-1994 timeframe are fairly weak, though these trends are a bit stronger when extending the CORE forcing to 2003 (Fig. S2). Surface trends in all three carbonate variables are comparable across all time frames, with slightly higher trends from 1998-2022 for pH and $[H^+]$. Notably, annual bottom $\Omega_{arag} < 1$ conditions first emerge in 2008, and
395 after 2020 stay below 1 for the remainder of the model simulation. Furthermore, bottom pH values are approaching 7.8 (e.g. conditions demonstrated to negatively affect growth and survival of red king crab) by the end of the model simulation.

Annual average surface Ω_{arag} and pH values from 1998-2022 are generally greater on the middle and outer shelf domains compared to the inner shelf domain (Fig. 7-8). Conversely,
400 bottom water values for both variables are generally greater for the inner shelf domain compared to the middle and outer shelf domains. The lowest bottom values tend to occur in the northwest Bering Sea shelf, in the Gulf of Anadyr. Relatively lower values of surface Ω_{arag} and pH are also apparent near the Yukon River delta. Most shelf surface waters have annual $\Omega_{arag} > 1.25$ and pH ≥ 8.0 . Bottom waters, however, are near or below the aragonite saturation horizon (i.e. $\Omega_{arag} = 1$)
405 for most of the middle and outer shelf, along with pH values < 8.0 and near 7.8 for the northwestern middle shelf domain. Surface Ω_{arag} and pH trends are spatially fairly consistent throughout the shelf, with slightly stronger, negative trends over the middle shelf and in the northwestern shelf near the Gulf of Anadyr (Fig. 7-8). Bottom water trends for both variables are more spatially heterogenous, with substantially greater trends on the outer shelf domain
410 compared to the rest of the shelf. This region, along with parts of the southeastern middle shelf domain, displays stronger, negative trends at the bottom compared to the surface, similar to the shelf-wide averaged timeseries plots in Fig. 6. $[H^+]$ trends display similar spatial patterns as pH and are not shown here.

Vertical profiles of modeled pH at the M2 and M8 mooring locations highlight the onset
415 of seasonally occurring pH values < 7.8 (Fig. 9). At M2, these conditions do not occur in the hindcast until after 2005, at which point they seasonally occur somewhat regularly, and shoal to depths between 30-50m. At M8, pH < 7.8 waters rarely occur prior to 2000, after which they occur seasonally every year. Most years, these conditions also shoal to 30-50m, however, there are several years when they occur throughout the entire water column.

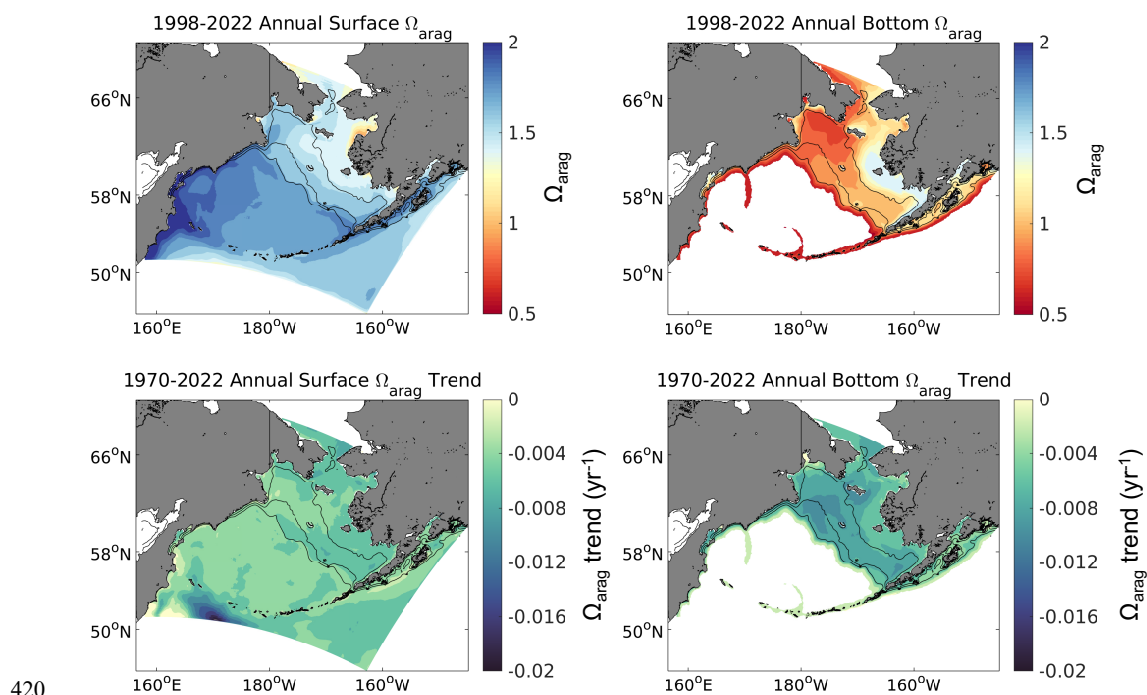


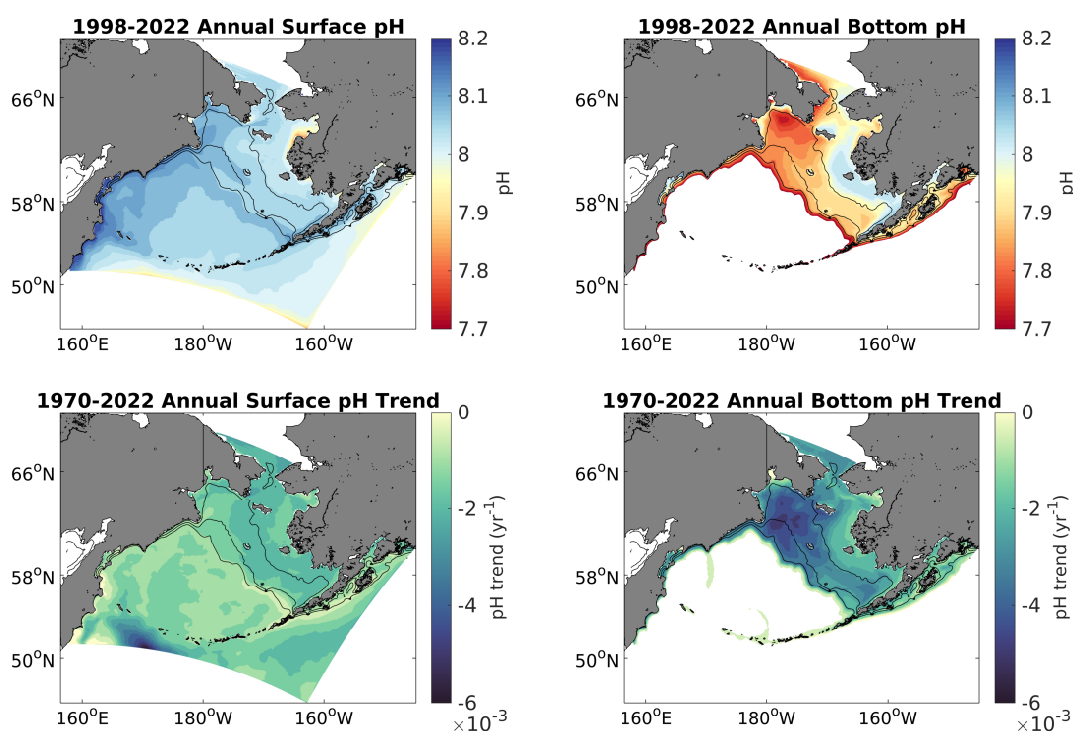
Figure 7: Spatial plots of model annual average surface (left) and bottom (right) Ω_{arag} from 1998-2022 (top) along with the linear trend for each grid cell (bottom) over the same timeframe. Bottom waters with depths > 1500m are omitted here as our focus is on the shelf.

3.4 Bering Sea Shelf Carbon Cycle

425 Atmospheric CO_2 concentrations significantly increase from 328 μatm in 1970 to 420
 μatm by 2022, while the surface ocean $p\text{CO}_2$ for the Bering Sea shelf increases from 324 μatm in
 1970 to 402 μatm in 2022 (Fig. 10a). This lag in the growth rate of surface ocean $p\text{CO}_2$
 compared to the atmosphere generates a net decrease in $Dp\text{CO}_2$ (i.e. $p\text{CO}_2^{\text{ocean}} - p\text{CO}_2^{\text{atmo}}$) and
 drives a more negative air-sea CO_2 flux, where a negative flux indicates a flux of carbon into the
 430 ocean (Fig. 10b, c). However, the more negative $Dp\text{CO}_2$ values with greater carbon fluxes into
 the ocean tend to occur from 1995-2022, following the switch from CORE to CFSR forcing.
 Indeed, analysis of the CORE-extended hindcast indicates that the switch in forcing plays a
 significant role, with the CORE forcing suggesting higher oceanic surface $p\text{CO}_2$ values and more
 positive CO_2 flux values during the overlapping years (Fig. S3). Furthermore, while there is a
 435 negative trend in CO_2 flux over the entire 1970-2022 timeframe (under combined forcing), there
 is a very minimal negative trend over the 1970-2003 CORE forced timeframe and a slight
 positive trend over the 1998-2022 CFSR forced timeframe, indicating that the transition in

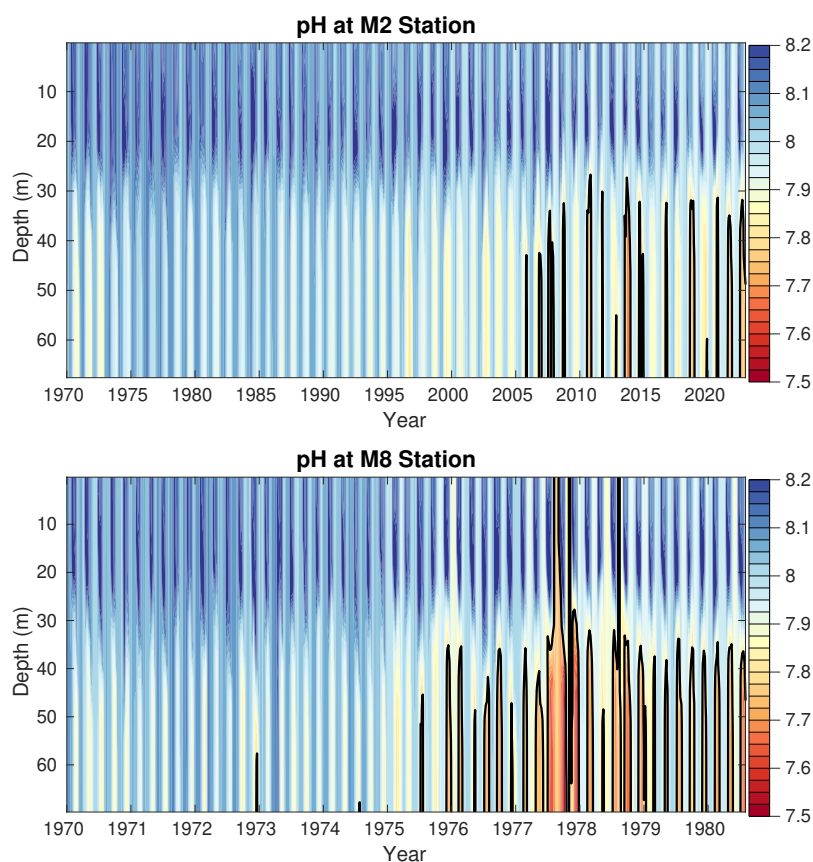


440 forcing is biasing the 1970-2022 trend (Fig. S3). To further illustrate this difference, we calculate the total carbon shelf sink using the spatial area of the shelf (i.e. area defined in Fig. 1; 804,393 km²). For the CORE-forced 1970-1994 timeframe, the shelf was an annual carbon sink of 1.1 TgC/year, compared to an annual carbon sink of 7.9 TgC/year for the 1998-2022 CFSR-forced timeframe.



445 **Figure 8:** Spatial plots of model annual average surface (left) and bottom (right) pH from 1998-2022 (top) along with the linear trend for each grid cell (bottom) over the same timeframe. Bottom waters with depths > 1500m are omitted here as our focus is on the shelf.

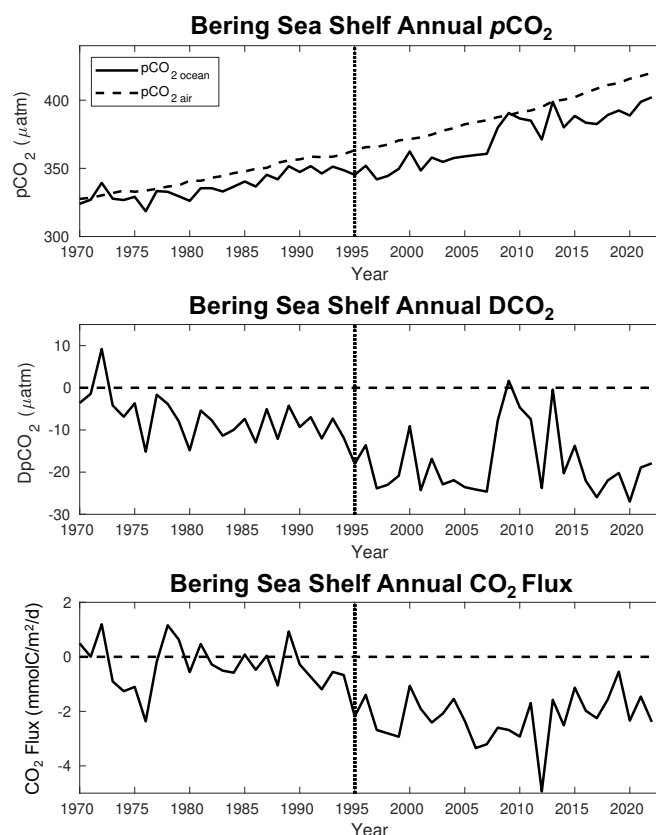
450 Figure 11 illustrates that a substantial amount of this annual carbon uptake occurs within the middle and outer shelf domain and the northern Bering Sea inner shelf domain. Conversely, coastal waters near regions of significant riverine runoff (e.g. Yukon and Kuskokwim Rivers) are an annual net carbon source. The spatial patterns of air-sea CO₂ flux are largely consistent with the spatial pattern in *Dp*CO₂, though there are some areas where the two variables are not aligned (i.e. not the same sign). This is especially apparent for the off-shelf Bering Sea Basin, which displays slightly negative *Dp*CO₂ values, but a relatively strong, positive (i.e. flux out of the



455 **Figure 9:** Model monthly averaged pH over the entire model timeseries at the M2 (top) and M8 (bottom) approximate model locations. The black contour line denotes the threshold for pH values < 7.8, which are conditions harmful to red king crab.

ocean) CO₂ flux. The difference in both variables between the CFSR and CORE forcing timeframes illustrates the substantial changes noted in Fig. 10. The off-shelf Bering Sea Basin in particular displays substantially greater magnitude, negative $DpCO_2$ and CO₂ flux values during
 460 the CFSR-forced timeframe. CO₂ flux values on the outer shelf domain and near the shelf-break are also substantially more negative (i.e. greater carbon uptake) during the CFSR-forced timeframe.

To further investigate the processes leading to the enhanced ocean carbon uptake, we examine the progression of the seasonal carbon cycle over each model decadal timeframe (Fig.
 465 12). These figures reveal a non-uniform seasonal increase in surface ocean pCO_2 , with the summer (May-September) values increasing at a much lower rate compared to the rest of the year. For example, the seasonal pCO_2 summer minimum increases by only 22 μatm over the



470 **Figure 10:** Timeseries of model annual average (top) surface ocean $p\text{CO}_2$ (black line) and atmospheric CO_2 concentration (dashed line), $\text{D}p\text{CO}_2$ (middle), and CO_2 flux (bottom). Here, $\text{D}p\text{CO}_2$ is defined as $p\text{CO}_{2,\text{ocean}} - p\text{CO}_{2,\text{atmo}}$ and a negative CO_2 flux signifies a flux of carbon into the ocean. The dotted line denotes the year where the forcing transitions from CORE to CFSR.

model timeframe, whereas the seasonal winter maximum in January increases by $93 \mu\text{atm}$.

475 Atmospheric $p\text{CO}_2$ also increases over this timeframe, but with minimal changes in seasonality (i.e. the seasonal amplitude increases by $\sim 6 \mu\text{atm}$ over the entire timeframe). The overall effect is a slight reduction in positive CO_2 flux (i.e. less carbon efflux to the atmosphere) during the months when the shelf is a net source of carbon (November-March) but generates greater magnitude, negative $\text{D}p\text{CO}_2$ and CO_2 flux values during the months when the shelf is a net carbon sink (April-September). Notably, these enhanced negative $\text{D}p\text{CO}_2$ and CO_2 flux values occur following the transition to CFSR-forcing.

480 To further understand changes in $p\text{CO}_2$, we separate the $p\text{CO}_2$ signal into a temperature component and non-temperature component following Takahashi et al., (2002):

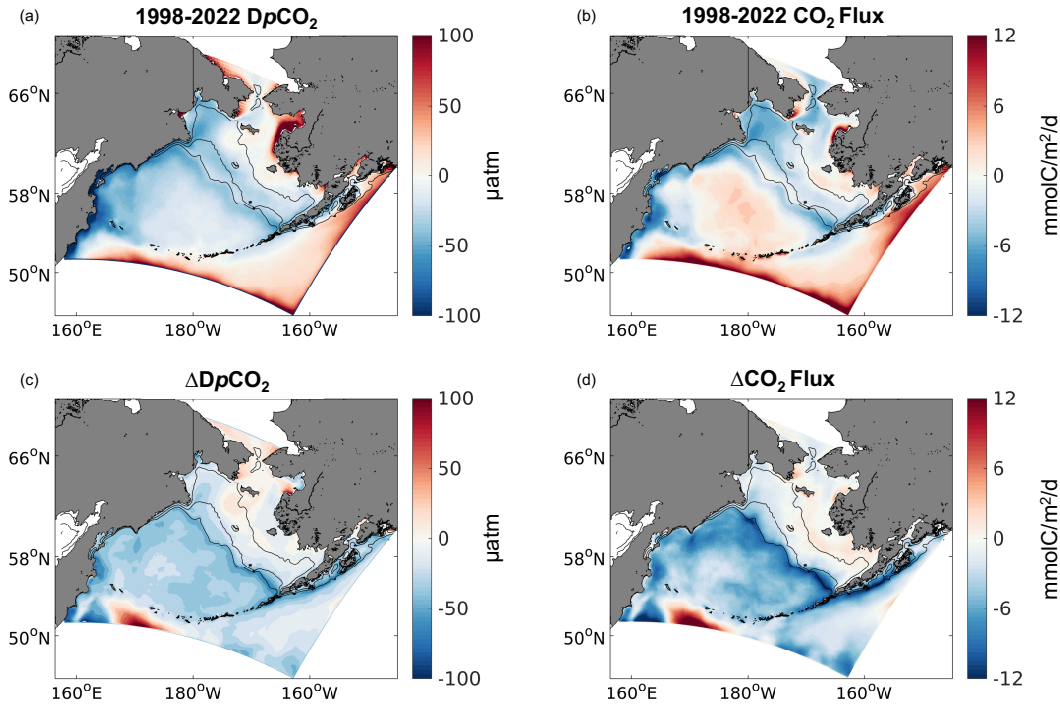


Figure 11: Spatial plots of model annual average surface (a) $DpCO_2$ and (b) CO_2 flux from 1998-2022. Also shown is (c) $\Delta DpCO_2$ and the (d) ΔCO_2 flux calculated as the difference between the 1998-2022 and the 1970-1994 timeframes.

485

$$pCO_{2T} = \overline{pCO_2} * \exp[0.0423(T - \bar{T})] \quad (5)$$

$$pCO_{2nonT} = pCO_2 * \exp[0.0423(\bar{T} - T)] \quad (6)$$

where the overbars represent the model annual mean values, pCO_{2T} is the temperature component reflecting the effect of thermal solubility on pCO_2 , while pCO_{2nonT} is the remaining pCO_2 effects governed by non-thermal components, including biological activity. Following equations 5 and 6, we can calculate the seasonal amplitude of both pCO_{2T} and pCO_{2nonT} , which gives an indication of which component has a greater effect on determining the seasonal pCO_2 . Figure 13 illustrates this comparison throughout the model timeframe. The seasonal amplitudes for both pCO_{2T} and pCO_{2nonT} increase over the model simulation, however, the amplitude for

490

495

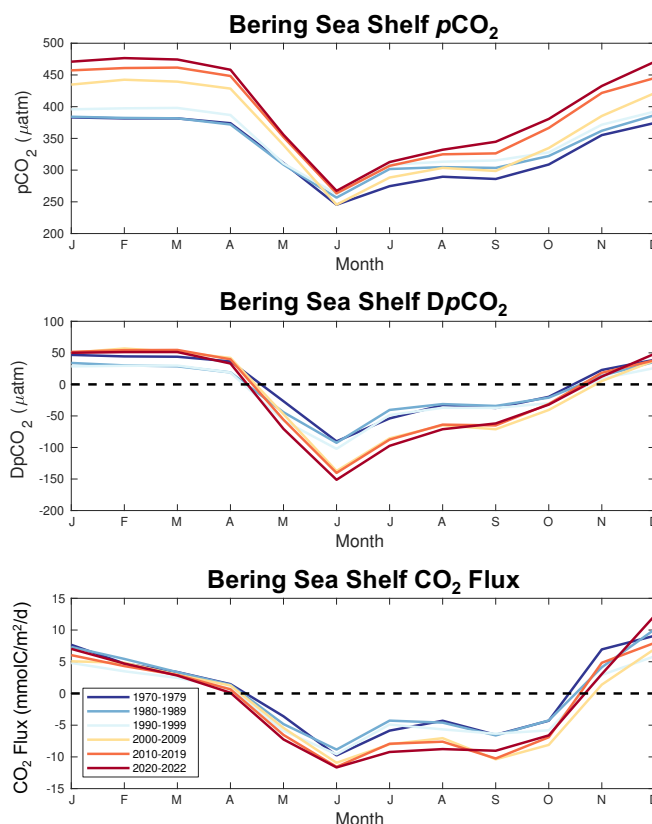


Figure 12: Seasonal plots of model surface ocean $p\text{CO}_2$ (top), DpCO_2 (middle), and CO_2 flux (bottom) averaged over multiple timeframes.

500 $p\text{CO}_2_{\text{nonT}}$ increases to a much greater extent. Furthermore, the $p\text{CO}_2_{\text{nonT}}$ amplitude is always greater than the $p\text{CO}_2_{\text{T}}$ amplitude, with the ratio increasing to greater than two.

Figure 6 illustrates that linear trends in Ω_{arag} and pH are greater at the bottom compared to the surface, especially for the CFSR-forced timeframe. Figure 14 demonstrates that this is also true for the trend in DIC, where the bottom trend over the entire model hindcast is a little
 505 over twice as strong compared to the surface. The CORE and CFSR forcing comparison illustrates that this enhanced bottom trend is a result of the CFSR-forced timeseries which is a factor of ~ 1.5 greater at the bottom compared to the surface for 1998-2022. Conversely, the CORE-forced surface trend is more than three times as strong as the bottom trend. However, extending the CORE forcing to 2003 doubles the bottom DIC trend, reducing this surface to
 510 bottom trend comparison to less than a factor of two (Fig. S4). There are also positive trends in integrated primary production and bottom water remineralization, along with a negative trend in

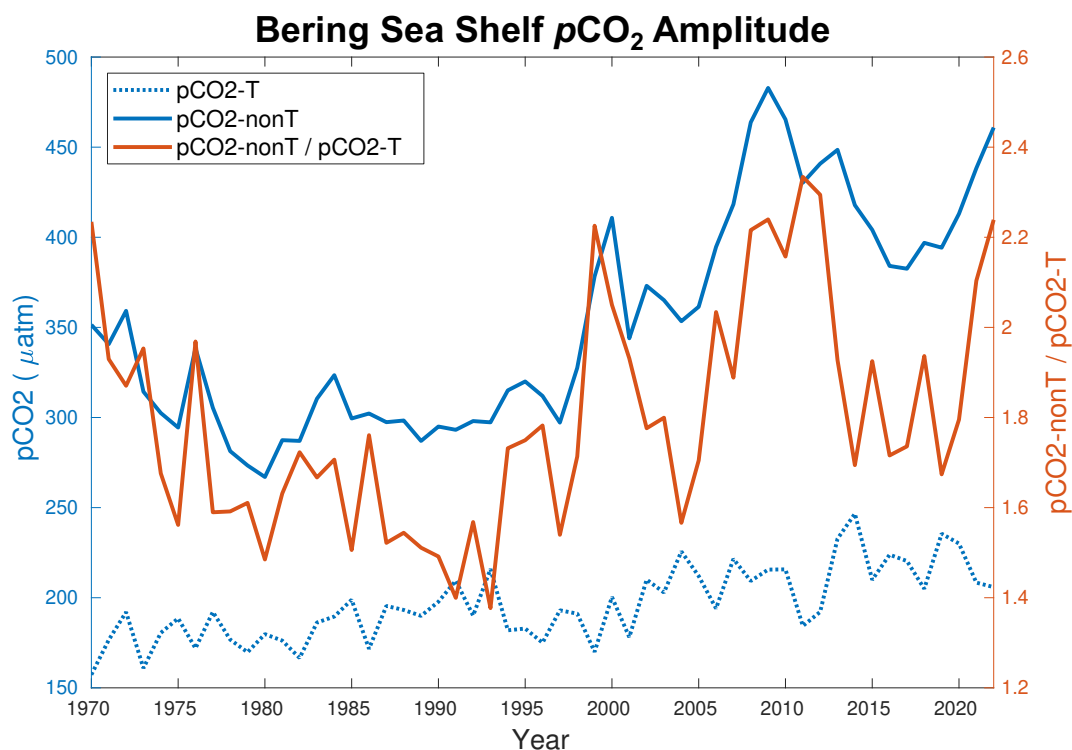
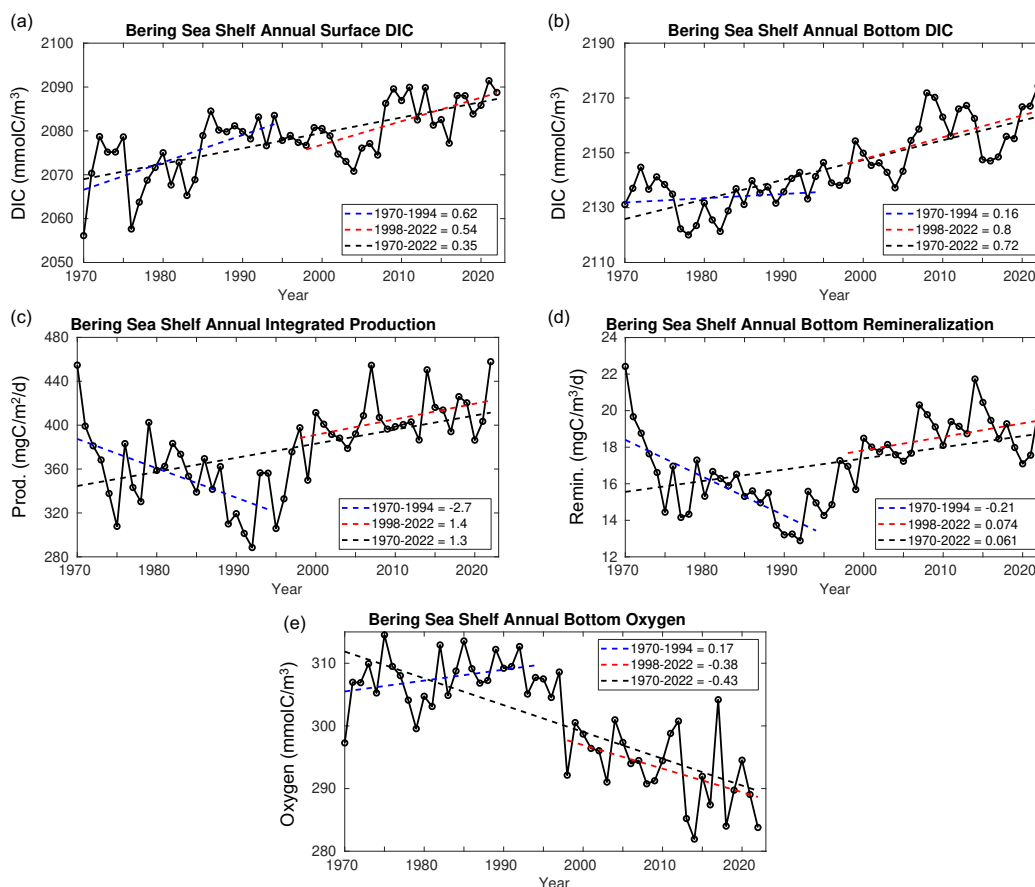


Figure 13: Timeseries of the yearly maximum seasonal amplitude of $p\text{CO}_2\text{-T}$ (blue dotted line), $p\text{CO}_2\text{-nonT}$ (solid blue line), and the ratio of $p\text{CO}_2\text{-nonT} / p\text{CO}_2\text{-T}$ (orange line).

515 bottom oxygen concentrations over the entire model timeframe. Here, primary production refers to gross primary production (GPP) and remineralization encompasses all detrital remineralization and benthic excretion. Productivity and remineralization rates are both relatively high to start the model simulation, before decreasing to a minimum in the early 1990s, and then steadily increasing through the remainder of the model simulation. This leads to opposite trends in all

520 three variables between the CORE and CFSR forced timeframes, with CORE trending towards lower productivity, remineralization, and higher oxygen, but CFSR trending towards higher productivity, remineralization and lower oxygen. However, the CORE trends are more affected by the relatively anomalous initial values, and the extended CORE-forced simulation also suggests a shift towards higher productivity and remineralization, though not to the same extent

525 as the overlapping CFSR-forced years (Fig. S4). Over the entire model hindcast, productivity is strongly correlated with bottom remineralization ($R = 0.92$) and negatively correlated with bottom oxygen ($R = -0.76$).



530 **Figure 14:** Timeseries plots of Bering Sea shelf model annual average (a) surface DIC, (b) bottom DIC, (c) depth integrated primary productivity, (d) bottom water remineralization, and (e) bottom water oxygen concentration. Also shown are the linear trend values over three different timeframes.

4 Discussion

Our model hindcast simulates surface Ω_{arag} and pH trends of $-0.043 \text{ decade}^{-1}$ and $-0.014 \text{ decade}^{-1}$ and bottom Ω_{arag} and pH trends of $-0.066 \text{ decade}^{-1}$ and $-0.028 \text{ decade}^{-1}$ respectively from 1970-2022 for the Bering Sea shelf. This surface pH trend is comparable to the global observed mean pH decline over a similar timeframe due to ocean acidification (Lauvset et al., 2015; Ma et al., 2023). Our surface Ω_{arag} trend is lower than the global observed Ω_{arag} trend of $-0.071 \text{ decade}^{-1}$ (Ma et al., 2023), though the global high latitude trend is more comparable to our model trend. 540 Pilcher et al., (2022) projected that surface Ω_{arag} on the Bering Sea shelf would decline by -0.044 to $-0.097 \text{ decade}^{-1}$ from 2010-2100 under the RCP 4.5 and RCP 8.5 emissions scenarios



respectively, while surface pH would decline by -0.015 to -0.04 decade⁻¹. Thus, our hindcast simulation has a historical acidification rate from 1970-2022 that is comparable to the projected RCP 4.5 acidification rate. Conversely, the RCP 8.5 acidification rate is more than twice as great
545 as our historical rate. This comparison provides context for the rate of change in carbonate chemistry that marine ecosystems have already experienced compared to the projected rate over the 21st Century.

Surface trends in Ω_{arag} are comparable across all model timeframes, while surface trends in pH and $[\text{H}^+]$ are stronger over the last 25 years, reflecting a recent increase in the rate of
550 acidification likely driven by the increased rate of atmospheric CO₂ growth. Interannual variability in surface carbonate variables also increased over the past 25 years, including the emergence of multi-year periods of sustained anomalous conditions. This is especially apparent for surface Ω_{arag} , with periods of relatively high (e.g. 2001-2007 and 2014-2019) and low (e.g. 2008-2013) Ω_{arag} conditions. This coincides with the observed warm and cold temperature
555 “stanzas” that have emerged for the Bering Sea shelf (Stabeno et al., 2012; Stabeno and Bell 2019). For the surface and bottom, warm temperatures lead to higher Ω_{arag} values while cold temperatures generate lower Ω_{arag} values. Pilcher et al., (2019) noted a similar phenomenon between a warm and cold temperature regime and attributed this to a combination of the thermal solubility effect on Ω_{arag} (i.e. cooling decreases Ω_{arag}) and increased fall productivity and ocean
560 carbon uptake. In our study, thermal solubility is likely also a contributor to recent Ω_{arag} variability; however, surface DIC (Fig. 14a) also displays a similar pattern between warm and cold temperature regimes suggesting the influence of changes in biogeochemistry (i.e. Pilcher et al., 2019). The warm and cold regimes also generate substantial differences in sea ice extent, which can impact the seasonal carbon cycle through changes in air-sea flux inhibition, the timing
565 and composition of the spring phytoplankton bloom, and changes in the sea ice carbonate pump (e.g. Mortenson et al., 2020). A complete mechanistic breakdown of how the warm and cold temperatures regimes impact the seasonal carbon cycle and modify background OA rates is beyond the scope of this present manuscript but is the focus of planned future work.

The threat OA presents to Alaskan marine ecosystems demonstrates a clear need to
570 develop accurate and reliable model-based OA products to support fisheries management. The recent emergence of multi-year anomalously low Ω_{arag} and pH conditions is significant because marine organisms may not be as resilient to longer cumulative exposure to acidic conditions

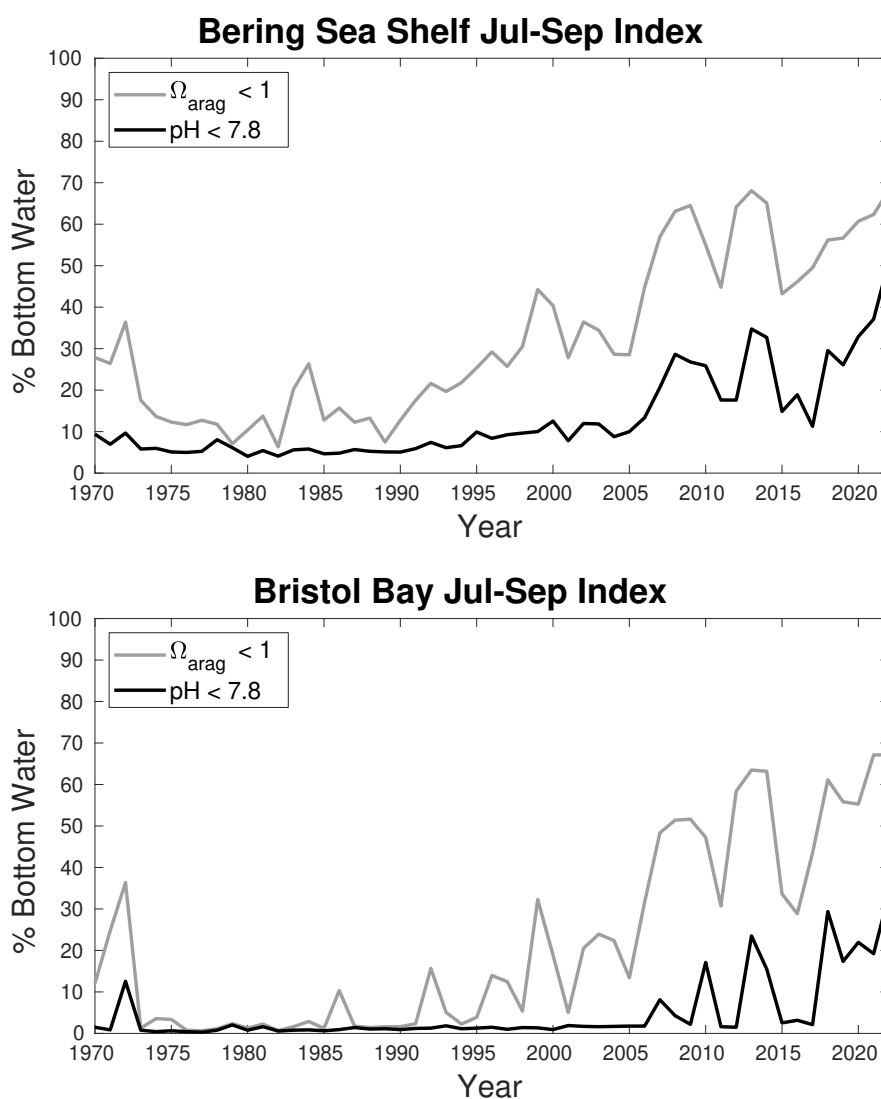


(Bednarsek et al., 2022). Furthermore, OA is gradually shifting waters to a lower Ω_{arag} and pH baseline and reduced buffer capacity, leading to a higher rate of extreme acidity events (Burger et al., 2020) and an amplification of the seasonal cycle (Kwiatkowski and Orr, 2018). It is therefore critical to track the development of high acidity water conditions on seasonal to annual timeframes to support tactical advice within the fisheries management process. To this end, we have developed an OA index for the Eastern Bering Sea shelf using annually updated output from our model hindcast (Fig. 15). This index indicates the area extent of the Bering Sea shelf where bottom waters are below threshold values of Ω_{arag} and pH from July-September. We specifically target summer bottom waters because this is when the seasonal bottom water respiration signal is greatest, thereby generating the most acidic seasonal conditions. The two biological thresholds are chosen as the aragonite saturation horizon, and a pH of 7.8, which has negative effects to red king and tanner crab growth and survival (Long et al., 2013a, b; Long et al., 2016). The spatial extent for both indices has greatly expanded over our model hindcast for both the entire Bering Sea shelf (Fig. 15a) and Bristol Bay (Fig. 15b), the location of a highly valuable red king crab fishery. Prior to 2005, between 5-10% of the shelf had pH < 7.8 conditions but by 2022 this jumped to more than 50% of the shelf spatial area. Thus, locations on the shelf that had rarely or never contained these conditions in our model hindcast prior to the early 2000s now regularly experience them (Fig. 9). Currently this index, along with spatial plots highlighting pH conditions on the shelf for the current year, are included in the annual NOAA Eastern Bering Sea Ecosystem Status Report (Siddon et al., 2022), a key report used by the North Pacific Fisheries Management Council for setting quotas.

Modeled bottom water acidification rates on the Bering Sea shelf are substantially greater compared to the surface, particularly for pH and $[\text{H}^+]$. The bottom water amplified trends emerge over the past 25 years, coinciding with a net increase in primary productivity, and a subsequent increase in bottom water remineralization. The accumulation of anthropogenic carbon can also generate relatively greater changes in pH and $[\text{H}^+]$ in subsurface waters due to nonlinearities in the carbonate system (Fassbender et al., 2023), though anthropogenic carbon is not explicitly tracked in our model simulations. Our model results add to a growing body of literature suggesting that biological remineralization reduces water buffer capacity and can accelerate subsurface acidification rates (Cai et al., 2011; Feely et al., 2010; Cross et al., 2018; Kwiatkowski et al., 2020; Arroyo et al., 2022; Qi et al., 2022; Fassbender et al., 2023). Indeed,



Qi et al., (2022) found accelerated OA rates in the neighboring Chukchi Sea due to enhanced
605 subsurface biological remineralization. Previous observational studies have also noted a long-
term increase in primary productivity for both the Arctic Ocean (Lewis et al., 2020) and the
Bering Sea (Wang et al.,



610 **Figure 15:** Timeseries plots of an OA indicator calculated as the spatial extent (i.e. percent of total area) of bottom waters with a July-September $\Omega_{\text{arag}} < 1$ (grey line) and $\text{pH} < 7.8$ (black line). The total spatial area is the entire Bering Sea shelf for the top plot and Bristol Bay for the bottom plot.

2022). Higher productivity in the Bering Sea has also been observed in warmer years (Lomas et al., 2020), though model projections suggest that overall phytoplankton biomass will decrease



with future climate warming (Cheng et al., 2021). Thus, the enhanced productivity may be a
615 transient response to recent observed warming and sea ice decline and the resulting ongoing
ecological shift (Moore and Stabeno 2015; Overland et al., 2023). Interestingly, Pilcher et al.,
(2022) did not find accelerated bottom water acidification rates compared to the surface in their
projected OA rates for the Bering Sea shelf. These projections were generated using the same
Bering10K-BESTNPZ model presented in here, suggesting that the enhanced bottom OA rates in
620 our hindcast result from the model forcing.

Here, we find that the Bering Sea shelf is an annual carbon sink of 1.1 – 7.9 TgC/year,
with the range resulting from the change in forcing between CORE and CFSR. Most of this
carbon uptake occurs on the middle and outer shelf domains, while the inner shelf domain
contains some regions of net carbon efflux, mostly located near river runoff. Previous estimates
625 for the shelf carbon sink have ranged from 2 – 67 TgC/year, and our estimate agrees with the 6.8
TgC/year estimate by Cross et al., (2013) that incorporated late fall/winter data when the shelf is
typically outgassing carbon. Notably, this range is significantly less than the previous model
estimate of 15-25 TgC/year by Pilcher et al., (2019), which was over a much shorter timeframe
(2003-2012) that only used the CFSR forcing (i.e. more comparable to our upper 7.9 TgC/year
630 estimate here). Using $p\text{CO}_2$ data from autonomous vehicles, Wang et al., (2022) found that
Bering Sea shelf carbon uptake has increased from 1989-2019 due to an increase in primary
productivity which suppressed summer $p\text{CO}_2$ values and generating more negative $Dp\text{CO}_2$. Our
model results present a similar mechanism (Fig. 12) but are highly uncertain as this mechanism
appears to be sensitive to the switch in forcing. The substantial increase in the magnitude of the
635 $p\text{CO}_2_{\text{nonT}}$ seasonal amplitude compared to $p\text{CO}_2_{\text{T}}$ may also indicate that changes in productivity
and respiration are driving recent changes in the model carbon cycle and the amplified bottom
water acidification rates. However, anthropogenic carbon uptake can also generate large changes
in the $p\text{CO}_2_{\text{nonT}}$ seasonal amplitude (Fassbender et al., 2018).

Interestingly, the strongest model trends over the past 25 years are in the off-shelf Bering
640 Sea Basin. This region is a net annual source of carbon (Fig. 11), but the model suggests that
this carbon efflux has substantially declined over the past 25 years. This region also displays
divergent $Dp\text{CO}_2$ and CO_2 flux patterns (i.e. negative $Dp\text{CO}_2$ but positive CO_2 flux) on annual
timeframes, likely due to the influence of wind speed in determining the magnitude of the flux.
For example, wind speeds in the Bering Sea basin are much stronger in winter compared to



645 summer, thus positive winter efflux values will be greater in magnitude than negative summer
influx values, generating a net positive annual average flux. However, our model results are
likely more uncertain for this region because the substantially greater depths combined with our
model terrain-following coordinates generate relatively deep surface grid cells, which may
significantly influence the air-sea gas exchange.

650 A noted caveat to our model results is that the shift in atmospheric and boundary
condition forcing in 1995 can lead to a shift in the system which impacts trends calculated over
the entire model timeframe. For some model variables such as salinity and air-sea CO₂ flux, the
impact is readily noticeable, particularly when extending the CORE forcing to 2003 (see
supplementary information). Conversely, the extent to which this switch impacts the trends in
655 Ω_{arag} and pH are less clear. Surface Ω_{arag} and pH trends are largely consistent across all three
timeframes, suggesting these trends are largely unaffected by the change in forcing. This result
is not unexpected, given that surface acidification rates are strongly tied to the atmospheric CO₂
concentration, which is not impacted by the forcing shift. There is a moderate acceleration of the
pH and [H⁺] trends over the last 25 years, however, the annual atmospheric CO₂ growth rate also
660 increases over this same timeframe. Meanwhile, bottom Ω_{arag} and pH display different trends
over the CORE and CFSR timeframes, with essentially no trend with the former but steep
negative trends with the latter. This result suggests that the 1970-2022 trend is not a product of a
discontinuity created in 1995 by the change in forcing, but rather emerges over the 1998-2022
CFSR forcing. Thus, the accelerated bottom OA rates generated by the model may be dependent
665 on the CFSR forcing, as they are driven by enhanced productivity-remineralization that is not
apparent in the CORE forced simulation. But it does not appear that these trends are artificially
generated by the switch in forcing itself.

It is also possible that these bottom water trends emerge over the more recent timeframe
and are independent of the forcing, a conclusion supported by previous observational studies
670 (e.g. Qi et al., 2022; Wang et al., 2022). Indeed, extending the CORE forced simulation to 2003
generates a modest increase in bottom water acidification rates. Diagnosing the mechanism
responsible for these differences in the forcing is beyond the scope of this manuscript, as our
goal is rather to highlight which variables and trends are impacted by the transition in forcing.
However, we note that the CORE atmospheric shortwave and longwave radiative forcing are
675 slightly adjusted to agree with the CFSR radiative forcing (Kearney et al., 2020) and that water



temperature comparisons between the two are comparable (Kearney 2021). Nonetheless, this study highlights the sensitivity of the simulated carbon cycle to small shifts in surface and boundary forcing and suggests that further constraints on the spinup and boundary condition forcing may be required as part of future model development.

680

5 Conclusions

We use a regional ocean biogeochemical model to simulate the Bering Sea shelf carbon cycle from 1970-2022. Over this timeframe, surface waters acidify at rates comparable to those observed in the global ocean, with a slight acceleration in the trend over the past 25 years. Shelf
685 bottom waters acidify at two to nearly three times the rate of surface waters, driven by increased productivity and subsurface respiration and remineralization. This mechanism leads to a substantial increase in the spatial extent of summer bottom waters with $\Omega_{\text{arag}} < 1$ and pH conditions harmful to red king crab, including parts of the shelf where these conditions previously did not occur during our model timeframe. To facilitate tracking these conditions and
690 support the fisheries management process, we have developed an OA index which is annually updated and presented as part of the NOAA Eastern Bering Sea Ecosystem Status Report. Lastly, we find that the Bering Sea shelf is an annual carbon sink of 1.1-7.9 TgC/year, which is lower than a previous model estimate of 15-25 TgC/year but is more consistent with the observational constraint of 6.8 TgC/year. The range in our estimate results from differences
695 between the two atmospheric forcing reanalysis products, with the higher estimate driven by relatively greater carbon uptake in summer and early fall and somewhat less winter carbon efflux.

Code and data availability

700 The ROMS Bering10K model source code is available on Github here <https://github.com/beringnpz/roms-bering-sea>, and the model output is available on the PMEL THREDDS server through the Alaska Climate Integrated Modeling Project https://data.pmel.noaa.gov/aclim/thredds/catalog/files/B10K-K20P19_CORECFS.html. Atmospheric CO₂ values for Barrow and Mauna Loa are publicly available at the NOAA Earth
705 System Research Laboratories Global Monitoring Laboratory. M2 mooring pCO₂ data are



available at the NOAA National Centers for Environmental Information (NCEI)

<https://www.ncei.noaa.gov/data/oceans/ncei/ocads/metadata/0157599.html>.

Author contributions

710 DJP and JNC conceptualized the project and acquired the funding. DJP ran the model
simulations and conducted the formal analysis, with assistance in model code development and
forcing generation from KAK, AJH, and WC. KAK, AJH, and WC provided data curation for
the model software and output. JNC, NM, and LM assisted with the observational data and
methodology for model validation. DJP generated the figures with assistance from LM. JNC
715 and WC provided project administration support. DJP prepared the manuscript, and all authors
commented on and contributed to the manuscript writing.

Competing interests

The authors declare that they have no conflict of interest.

720

Acknowledgements

This work was facilitated through the use of advanced computational, storage, and
networking infrastructure provided by the Hyak supercomputer system at the University of
Washington. Stimulating conversations about the model output were also provided by our
725 colleagues at the UW Cooperative Institute for Climate, Ocean, and Ecosystem Studies, and the
PMEL Carbon and Eco-FOCI Groups. Funding for this project was provided by the NOAA
Ocean Acidification Program (Research Organization Registry # 02bfn4816, NRDD # 20780)
through the Cooperative Institute for Climate, Ocean, and Ecosystem Studies under NOAA
Cooperative Agreement NA20OAR4320271. This is CICOES contribution 2024-1354, PMEL
730 contribution 5619, EcoFOCI-1051, and PNNL-SA-197834.



References

- Algayer, T., Mahmoud, A., Saksena, S., Long, W.C., Swiney, K.M., Foy, R.J., Steffel, B.V.,
Smith, K.E., Aronson, R.B., and Dickinson, G.H.: Adult snow crab, *Chionoecetes opilio*,
735 display body-wide exoskeletal resistance to the effects of long-term ocean acidification,
Marine Biology, 170:63, doi:10.1007/s00227-023-04209-0, 2023.
- Arroyo, M.C., Fassbender, A.J., Carter, B.R., Edwards, C.A., Fiechter, J., Norgaard, A., and
Feely, R.A.: Dissimilar sensitivities of ocean acidification metrics to anthropogenic carbon
740 accumulation in the Central North Pacific Ocean and California Current Large Marine
Ecosystem, Geophys. Res. Lett., 49, e2022GL097835, doi:10.1029/2022GL097835, 2022.
- Bates, N. R., Mathis, J. T., and Jeffries, M. A.: Air-sea CO₂ fluxes on the Bering Sea shelf,
Biogeosci., 8, 1237–1253, doi: 10.5194/bg-8-1237-2011, 2011.
- Bednarsek, N., Tarling, G. A., Bakker, D. C. E., Fielding, S., Jones, E. M., Venables, H. J., et al.:
745 Extensive dissolution of live pteropods in the Southern Ocean, Nat. Geosci. 5, 881–885,
doi: 10.1038/NGEO1635, 2012.
- Bednarsek, N., Beck, M.W., Pelletier, G., Applebaum, S.L., Feely, R.A., Butler, R., Byrne, M.,
Peabody, B., Davis, J., and Strus, J.: Natural Analogues in pH Variability and Predictability
across the Coastal Pacific Estuaries: Extrapolation of the Increased Oyster Dissolution
under Increased pH Amplitude and Low Predictability Related to Ocean Acidification,
750 Environ. Sci. Technol., 56, 12, 9015-9028, doi:10.1021/acs.est.2c00010, 2022.
- Bianucci, L., Denman, K.L., and Ianson, D.: Low oxygen and high inorganic carbon on the
Vancouver Island Shelf, J. Geophys. Res., 116, C07011, doi:10.1029/2010JC006720, 2011.
- Burger, F.A., Frölicher, T.L., and John, J.G.: Increase in ocean acidity variability and extremes
under increasing atmospheric CO₂, Biogeosci., 17, 4633-4662, doi:10.5194/bg-17-4633-
755 2020, 2020.
- Cai et al.: Acidification of subsurface coastal waters enhanced by eutrophication, Nat. Geosci. 4,
766-770, doi:10.1038/NGEO1297, 2011.
- Cheng, W., Hermann, A.J., Hollowed, A.B., Holsman, K.K., Kearney, K.A., Pilcher, D.J., Stock,
C.A., and Aydin, K.Y.: Eastern Bering Sea shelf environmental and lower trophic level
760 responses to climate forcing: Results of dynamical downscaling from CMIP6, Deep-Sea
Res. II, 193, 104975, doi:10.1016/j.dsr2.2021.104975, 2021.
- Cross, J. N., Mathis, J. T., and Bates, N. R.: Hydrographic controls on net community production



- and total organic carbon distributions in the eastern Bering Sea, *Deep-Sea Res. II*, 6, 98–109, doi: 10.1016/j.dsr2.201202.003, 2012.
- 765 Cross, J. N., Mathis, J. T., Bates, N. R., and Byrne, R. H.: Conservative and non-conservative variations of total alkalinity on the southeastern Bering Sea shelf, *Mar. Chem.* 154, 110–112, doi: 10.1016/j.marchem.2013.05.012, 2013.
- Cross, J. N., Mathis, J. T., Lomas, M. W., Moran, S. B., Baumann, M. S., Shull, D. H., et al.: Integrated assessment of the carbon budget in the southeastern Bering Sea, *Deep-Sea Res. II*
- 770 109, 112–124, doi: 10.1016/j.dsr2.2014.03.003, 2014.
- Cross, Jessica N.; Monacci, Natalie M.; Musielewicz, Sylvia; Maenner Jones, Stacy,: High-resolution ocean and atmosphere pCO₂ time-series measurements from mooring M2_164W_57N in the Bering Sea (NCEI Accession 0157599). NOAA National Centers for Environmental Information. Dataset. https://doi.org/10.3334/cdiac/otg.tsm_m2_164w_57n.
- 775 [Accessed September 2023](https://doi.org/10.3334/cdiac/otg.tsm_m2_164w_57n), 2016.
- Cross, J.N., Mathis, J.T., Pickart, R.S., and Bates, N.R.: Formation and transport of corrosive water in the Pacific Arctic region, *Deep-Sea Res. II*, 152, 67-81, doi:10.1016/j.dsr2.2018.05.020, 2018.
- Danielson, S. L., Curchitser, E. N., Hedstrom, K. S., Weingartner, T. J., and Stabeno, P. J.: On
- 780 ocean and sea ice modes of variability in the Bering Sea, *J. Geophys. Res.* 116:C12034, doi: 10.1029/2011JC007389, 2011.
- Doney, S.C., Busch, S., Cooley, S.R., and Kroeker, K.: The Impacts of Ocean Acidification on Marine Ecosystems and Reliant Human Communities, *Annu. Rev. Environ. Resour.*, 45, 11.1-11.30, doi:10.1146/annurev-environ-012320-083019, 2020.
- 785 Fassbender, A.J., Sabine, C.L., and Palevsky, H.I.: Nonuniform ocean acidification and attenuation of the ocean carbon sink, *Geophys. Res. Lett.*, 44, 8404-8413, doi:10.1002/2017GL074389, 2017.
- Fassbender, A.J., Rodgers, K.B., Palevsky, H.I., and Sabine, C.L.: Seasonal Asymmetry in the Evolution of Surface Ocean pCO₂ and pH Thermodynamic Drivers and the Influence of
- 790 Sea-Air CO₂ Flux, *Global Biogeochem. Cycles*, 32, 1476-1497, doi:10.1029/2017GB005855, 2018.
- Fassbender, A.J., Orr, J.C., and Dickson, A.G.: Technical note: Interpreting pH changes, *Biogeosci.*, 18, 1407-1415, doi:10.5194/bg-18-1407-2021, 2021.



- 795 Fassbender, A.J., Carter, B.R., Sharp, J.D., Huang, Y., Arroyo, M.C., and Frenzel, H.: Amplified
Subsurface Signals of Ocean Acidification, *Global Biogeochem. Cycles*, 37,
e2023GB007843, doi:10.1029/2023GB007843, 2023.
- Fedewa, E., B. Garber-Yonts, K. Shotwell,: Ecosystem and Socioeconomic Profile of the Bristol
Bay Red King Crab stock. Appendix E. In J. Zheng and M.S.M. Siddeek. 2020. Bristol Bay
Red King Crab Stock Assessment in Fall 2020, tock assessment and fishery evaluation
800 report for the Bering Sea/Aleutian Islands king and Tanner crabs. North Pacific Fishery
Management Council, 1007 W 3rd Ave, Suite 400 Anchorage, AK 99501. 31 p. Available
online: https://meetings.npfmc.org/CommentReview/DownloadFile?p=ea0403bc-6544-4241-bf8c-b9c7a8ebf17d.pdf&fileName=SAFE_2020_App_E_BBRKC_ESP_2020.pdf,
2020.
- 805 Feely, R.A., Sabine, C.L., Lee, K., Berelson, W., Kleypas, J., Fabry, V.J., and Millero, F.J.:
Impact of Anthropogenic CO₂ on the CaCO₃ System in the Oceans, *Science*, 305, 363,
doi:10.1126/science.1097329, 2004.
- Feely, R. A., Sabine, C. L., Hernandez-Ayon, J. M., Ianson, D., and Hales, B.: Evidence for
upwelling of corrosive “acidified” water onto the continental shelf, *Science* 320, 1490–
810 1492, doi: 10.1126/science.1155676, 2008.
- Feely, R.A., Alin, S.R., Newton, J., Sabine, C.L., Warner, M., Devol, A., Krembs, C., and
Maloy, C.: The combined effects of ocean acidification, mixing, and respiration on pH and
carbonate saturation in an urbanized estuary, *Estuar. Coast. Shelf Sci.*, 88, 442-449,
doi:10.1016/j.ecss.2010.05.004, 2010.
- 815 Friedlingstein et al.: Global Carbon Budget 2020, *Earth Syst. Sci. Data*, 12, 3269-3340,
doi:10.5194/essd-12-3269-2020, 2020.
- Garcia, H. E., and Gordon, L. I.: Oxygen solubility in seawater: Better fitting equations, *Limnol.*
Oceanogr., 37(6),1307–1312, doi:10.4319/lo.1992.37.6.1307, 1992.
- Garcia, H. E., K. Weathers, C. R. Paver, I. Smolyar, T. P. Boyer, R. A. Locarnini, M. M. Zweng,
820 A. V. Mishonov, O. K. Baranova, D. Seidov, and J. R. Reagan: World Ocean Atlas 2018,
Volume 3: Dissolved Oxygen, Apparent Oxygen Utilization, and Oxygen Saturation, A.
Mishonov Technical Ed.; NOAA Atlas NESDIS 83, 38pp., 2018.
- Gibson, G. A., and Spitz, Y. H.: Impacts of biological parameterization, initial conditions, and
environmental forcing on parameter sensitivity and uncertainty in a marine ecosystem



- 825 model for the Bering Sea, *J. Mar. Syst.* 88(2), 214–231,
<https://doi.org/10.1016/j.jmarsys.2011.04.008>, 2011.
- Gruber et al.: The oceanic sink for anthropogenic CO₂ from 1994 to 2007, *Science*, 363, 1193–
1199, doi:10.1126/science.aau5153, 2019.
- Haidvogel, D. B., et al.: Ocean forecasting in terrain-following coordinates: Formulation and
830 skill assessment of the Regional Ocean Modeling System, *J. Comp. Phys.* 227(7), 3595–
3624, <https://doi.org/10.1016/j.jcp.2007.06.016>, 2008.
- Hauri, C., Pagès, R., McDonnell, A.M.P., Stuecker, M.F., Danielson, S.L., Hedstrom, K., Irving,
B., Schultz, C., and Doney, S.C.: Modulation of ocean acidification by decadal climate
variability in the Gulf of Alaska, *Comm. Earth Environ.* 2:191, 1-7, doi:10.1038/s43247-
835 021-00254-z, 2021.
- Hermann, A. J., Gibson, G. A., Bond, N. A., Curchitser, E. N., Hedstrom, K., Cheng, W., Wang,
M., Cokelet, E.D., Stabeno, P.J., Aydin, K.: Projected future biophysical states of the
Bering Sea, *Deep Sea Res. II*, 134, 30-47, <https://doi.org/10.1016/j.dsr2.2015.11.001>, 2016.
- Jolliff, J. K., Kindle, J. C., Shulman, I., Penta, B., Friedrichs, M. A. M., Helber, R., et al.:
840 Summary diagrams for coupled hydrodynamic-ecosystem model skill assessment, *J. Mar.*
Syst. 76, 64–82, doi: 10.1016/j.jmarsys.2008.05.014, 2009.
- Kearney, K. A.: Freshwater Input to the Bering Sea, 1950 – 2017, (NMFS-AFSC-388), 46, 2019.
- Kearney, K., Hermann, A., Cheng, W., Ortiz, I., Aydin, K.: A coupled pelagic-benthic-sympagic
biogeochemical model for the Bering Sea: documentation and validation of the BESTNPZ
845 model (v2019.08.23) within a high-resolution regional ocean model, *Geoscientific Model*
Development 13(2), 597–650, <https://doi.org/10.5194/gmd-13-597-2020>, 2020.
- Kearney, K. A.: Temperature data from the eastern Bering Sea continental shelf bottom trawl
survey as used for hydrodynamic model validation and comparison (U.S. Dep. Commer.,
NOAA Tech. Memo. No. NMFS-AFSC-415), 2021.
- 850 Khatiwala, S., Primeau, F., and Hall, T.: Reconstruction of the history of anthropogenic CO₂
concentrations in the ocean, *Nature* 462, 346–349, doi: 10.1038/nature08526, 2009.
- Kinder, T.H., Chapman, D.C., and Whitehead Jr., J.A.: Westward Intensification of the Mean
Circulation on the Bering Sea Shelf, *J. Phys. Oceanog.*, 16, 1217-1229, doi:10.1175/1520-
0485(1986)016<1217:WIOTMC>2.0.CO;2, 1986.
- 855 Kwiatkowski, L., and Orr, J.C.: Diverging extremes for ocean acidification during the twenty-



- first century, *Nature Climate Change*, 8, 141-145, doi:10.1038/s41558-017-0054-0, 2018.
- Kwiatkowski, L., et al.: Twenty-first century ocean warming, acidification, deoxygenation, and upper-ocean nutrient and primary productivity decline from CMIP6 model projections, *Biogeosci.*, 17, 3439-3470, doi:10.5194/bg-17-3439-2020, 2020.
- 860 Large, W.G., and Yeager, S.G.: The global climatology of an interannually varying air-sea flux data set, *Clim. Dynam.*, 33, 341-364, 2009.
- Laurent, A., Fennel, K., Cai, W.-J., Huang, W.-J., Barbero, L., and Wanninkhof, R.: Eutrophication-induced acidification of coastal waters in the northern Gulf of Mexico: Insights into origin and processes from a coupled physical-biogeochemical model, *Geophys. Res. Lett.*, 44, 946-956, doi:10.1002/2016GL071881, 2017.
- 865 Lauvset, S.K., Gruber, N., Landschützer, P., Olsen, A., and Tjiputra, J.: Trends and drivers in global surface ocean pH over the past 3 decades, *Biogeosci.*, 12, 1285-1298, doi:10.5194/bg-12-1285-2015, 2015.
- Lewis, E. R., and Wallace, D. W. R.: Program Developed for CO₂ System Calculations. Rep. 870 BNL-61827, Oak Ridge, TN: U.S. Dep. of Energy, Oak Ridge Natl. Lab., Carbon Dioxide Inf. Anal. Cent., 1998.
- Lewis, K.M., van Dijken, G.L., Arrigo, K.R.: Changes in phytoplankton concentration now drive increased Arctic Ocean primary production, *Science*, 369, 198-202, doi:10.1126/science.aay8380, 2020.
- 875 Lomas, M.W., Eisner, L.B., Gann, J., Baer, S.E., Mordy, C.W., and Stabeno, P.J.: Time-series of direct primary production and phytoplankton biomass in the southeastern Bering Sea: response to cold and warm stanzas, *Mar. Ecol. Prog. Ser.*, 642, 39-54, doi:10.103354/meps13317, 2020.
- Long, W.C., Swiney, K.M., and Foy, R.J.: Effects of high pCO₂ on Tanner crab 880 reproduction and early life history, Part II: carryover effects on larvae from oogenesis and embryogenesis are stronger than direct effects, *ICES J. Mar. Sci.* 73 (3), 836–848, <https://doi.org/10.1093/icesjms/fsv251>, 2016.
- Long, W.C., Swiney, K.M., Harris, C., Page, H.N., and Foy, R.J.: Effects of ocean acidification on Juvenile Red king crab (*Paralithodes camtschaticus*) and tanner crab 885 (*Chionoecetes bairdi*) growth, condition, calcification, and survival, *PLoS One* 8 (4), e60959, <https://doi.org/10.1371/journal.pone.0060959>, 2013a.



- Long, W.C., Swiney, K.M., and Foy, R.J.: Effects of ocean acidification on the embryos and larvae of red king crab, *Paralithodes camtschaticus*, *Mar. Pollut. Bull.* 69, 38–47, <https://doi.org/10.1016/j.marpolbul.2013.01.011>, 2013b.
- 890 Ma, D., Gregor, L., and Gruber, N.: Four Decades of Trends and Drivers of Global Surface Ocean Acidification, *Global Biogeochem. Cycles*, 37, e2023GB007765, doi:10.1029/2023GB007765, 2023.
- Mathis, J. T., Cross, J. N., and Bates, N. R.: Coupling primary production and terrestrial runoff to ocean acidification and carbonate mineral suppression in the eastern Bering Sea, *J. Geophys. Res.* 116:C02030, doi: 10.1029/2010JC006453, 2011.
- 895 McKinley, G.A., Fay, A.R., Eddebbbar, Y.A., Gloege, L., and Lovenduski, N.S.: External forcing explains recent decadal variability of the ocean carbon sink, *AGU Advance*, 1, e2019AV000149, doi:10.1029/2019AV000149, 2020.
- Moore, S.E. and Stabeno, P.J.: Synthesis of Arctic Research (SOAR) in marine ecosystems of the Pacific Arctic, *Prog. Oceanogr.*, 136, 1-11, doi:10.1016/j.pocean.2015.05.017, 2015.
- 900 Mortenson, E., Steiner, N., Monahan, A.H., Hayashida, H., Sou, T., and Shao, A.: Modeled impacts of sea ice exchange processes on Arctic Ocean carbon uptake and acidification (1980-2015), *J. Geophys. Res. Oceans*, 125, e2019JC015782, doi:10.1029/2019JC015782, 2020.
- 905 Niemi, A., Bednarsek, N., Michel, C., Feely, R.A., Williams, W., Azetsu-Scott, K., Walkusz, W., and Reist, J.D.: Biological Impact of Ocean Acidification in the Canadian Arctic: Widespread Severe Pteropod Shell Dissolution in Amundsen Gulf, *Front. Mar. Sci.*, 8, 600184, doi:10.3380/fmars.2021.600184, 2021.
- Orr, J.C., Najjar, R., Sabine, C.L., and Joos, F.: Abiotic-HOWTO, Internal OCMIP Report, 25 pp., <https://www.cgd.ucar.edu/oce/OCMIP/HOWTO-Abiotic.pdf>, 1999.
- 910 Overland, J.E., Siddon, E., Sheffield, G., Ballinger, T.J., and Szuwalski, C.: Transformative ecological and human impacts from climate change and diminished sea ice in the northern Bering Sea, *Weather, Climate, and Society*, doi:10.1175/WCAS-D-23-0029.1, 2023.
- Pan-Arctic River Transport of Nutrients, Organic Matter, and Suspended Sediments Project [PARTNERS]: Arctic River Biogeochemistry Data Set, Available at <http://ecosystems.mbl.edu/partners/>, 2010.
- 915 Pilcher, D. J., Naiman, D. M., Cross, J. N., Hermann, A. J., Siedlecki, S. A., Gibson, G. A., and



- Mathis, J. T.: Modeled Effect of Coastal Biogeochemical Processes, Climate Variability,
and Ocean Acidification on Aragonite Saturation State in the Bering Sea, *Front. Mar. Sci.*,
920 5:508, <https://doi.org/10.3389/fmars.2018.00508>, 2019.
- Pilcher, D.J., Cross, J.N., Hermann, A., Kearney, K., Cheng, W., and Mathis, J.T.: Dynamically
downscaled projections of ocean acidification for the Bering Sea, *Deep-Sea Res. II*, 198,
105055, doi:10.1016/j.dsr2.2022.105055, 2022.
- Qi, D., Wu, Y., Chen, L., Cai, W.-J., Ouyang, Z., Zhang, Y., Anderson, L.G., Feely, R.A.,
925 Zhuang, Y., Lin, H., Lei, R., and Bi, H.: Rapid Acidification of the Arctic Chukchi Sea
Waters Driven by Anthropogenic Forcing and Biological Carbon Recycling, *Geophys. Res.
Lett.*, 49, e2021GL097246, doi:10.1029/2021GL097246, 2022.
- Saha, S., Moorthi, S., Wu, X., Wang, J., Nadiga, S., Tripp, P., et al.: The NCEP climate forecast
system reanalysis, *Bull. Am. Meteorol. Soc.* 91, 1015–1057, doi:
930 10.1175/2010BAMS3001.1, 2010.
- Saha, S., Moorthi, S., Wu, X., Wang, J., Nadiga, S., Tripp, P., et al.: The NCEP
climate forecast system version 2, *J. Climate* 27, 2185–2208, doi: 10.1175/JCLI-
D-12-00823.1, 2014.
- Shchepetkin, A. F., and McWilliams, J. C.: The regional oceanic modeling system (ROMS): A
935 split-explicit, free-surface, topography-following-coordinate oceanic model, *Ocean
Modelling* 9(4), 347–404, <https://doi.org/10.1016/j.ocemod.2004.08.002>, 2005.
- Siddon, E.C., Zador, S.G., and Hunt Jr., G.L.: Ecological responses to climate perturbations and
minimal sea ice in the northern Bering Sea, *Deep-Sea Res. II*, 181–182, 104914,
doi:10.1016/j.dsr2.2020.104914, 2020.
- 940 Siddon, E.: Ecosystem Status Report 2022: Eastern Bering Sea, Stock Assessment and
Fishery Evaluation Report, North Pacific Fishery Management Council, 1007 West 3rd
Ave., Suite 400, Anchorage, Alaska 99501, 2022.
- Siedlecki, S.A., Banas, N.S., Davis, K.A., Giddings, S., Hickey, B.M., MacCready, P., Connolly,
T., and Geier, S.: Seasonal and interannual oxygen variability on the Washington and
945 Oregon continental shelves, *J. Geophys. Res. Oceans*, 120, 608–633,
doi:10.1002/2014JC010254, 2015.
- Siedlecki, S.A., Pilcher, D., Howard, E.M., Deutsch, C., MacCready, P., Norton, E.L., Frenzel,



- H., Newton, J., Feely, R.A., Alin, S.R., and Klinger, T.: Coastal processes modify projections of some climate-driven stressors in the California Current System, *Biogeosci.*, 18, 2871-2890, doi:10.5194/bg-18-2871-2021, 2021.
- 950
- Stabeno, P. J., Kachel, N. B., Moore, S. E., Napp, J. M., Sigler, M., Yamaguchi, A., et al.: Comparison of warm and cold years on the southeastern Bering Sea shelf and some implications for the ecosystem, *Deep-Sea Res. II*, 6, 31–45, doi: 10.1016/j.dsr2.2012.02.020, 2012.
- 955
- Stabeno, P.J., Danielson, S.L., Kachel, D.G., Kachel, N.B., and Mordy, C.W.: Currents and transport on the Eastern Bering Sea shelf: An integration of over 20 years of data, *Deep-Sea Res. II*, 134, 13-29, doi:10.1016/j.dsr2.2016.05.010, 2016.
- Stabeno, P.J., and Bell, S.W.: Extreme conditions in the Bering Sea (2017-2018): Record-breaking low sea-ice extent, *Geophys. Res. Lett.*, 46, doi:10.1029/2019GL083816, 2019.
- 960
- Stow, C. A., Jolliff, J., McGillicuddy, D. J., Doney, S. C., Allen, J. I., Friedrichs, M. A. M., et al.: Skill assessment for coupled biological/physical models of marine systems, *J. Mar. Syst.* 76, 4–15, doi: 10.1016/j.jmarsys.2008.03.011, 2009.
- Striegl, R. G., Dornblaser, M. M., Aiken, G. R., Wickland, K. P., and Raymond, P. A.: Carbon export and cycling by the Yukon, Tanana, and Porcupine rivers, Alaska, 2001-2005, *Water Resources Research*, 43(2), 2001–2005, <https://doi.org/10.1029/2006WR005201>, 2007.
- 965
- Sutton, A.J., et al.: Autonomous seawater $p\text{CO}_2$ and pH time series from 40 surface buoys and the emergence of anthropogenic trends, *Earth Syst. Sci. Data*, 11, 421-439, doi:10.5194/essd-11-421-2019, 2019.
- Szuwalski, C.S., Aydin, K., Fedewa, E.J., Garber-Yonts, B., and Litzow, M.A.: The collapse of eastern Bering Sea snow crab, *Science*, 382, 306-310, doi:10.1126/science.adf6035, 2023.
- 970
- Takahashi, T., Sutherland, S.C., Sweeney, C., Poisson, A., Metzl, N., Tilbrook, B., Bates, N., Wanninkhof, R., Feely, R.A., Sabine, C., Olafsson, J., and Nojiri, Y.: Global sea-air CO_2 flux based on climatological surface ocean $p\text{CO}_2$ and seasonal biological and temperature effects, *Deep-Sea Res II*, 49, 1601-1622, doi:10.1016/S0967-0645(02)00003-6, 2002.
- 975
- Thoning, K.W., Crotwell, A.M. and Mund, J.W.: Atmospheric Carbon Dioxide Dry Air Mole Fractions from continuous measurements at Mauna Loa, Hawaii, Barrow, Alaska, American Samoa and South Pole. 1973-2021, Version 2022-05 National Oceanic and Atmospheric Administration (NOAA), Global Monitoring Laboratory (GML), Boulder, Colorado, USA



<https://doi.org/10.15138/yaf1-bk21>, 2022.

980 Wang, H., Lin, P., Pickart, R.S., and Cross, J.N.: Summer surface CO₂ dynamics on the Bering
Sea and eastern Chukchi Sea shelves from 1989 to 2019, *J. Geophys. Res. Oceans*, 127,
e2021JC017424, doi:10.1029/2021JC017424, 2022.

Wanninkhof, R.: Relationship between wind speed and gas exchange over the ocean revisited,
Limnology and Oceanography: Methods 12, 351–362,

985 <https://doi.org/10.4319/lom.2014.12.351>, 2014.

Wiese, F. K., Van Pelt, T. I., and Wiseman, W. J.: Bering Sea linkages, *Deep-Sea Res. II*, 6, 2–5,
doi: 10.1016/j.dsr2.2012.03.001, 2012.